Ann. Geophys., 27, 231–259, 2009
www.ann-geophys.net/27/231/2009/
© Author(s) 2009. This work is distributed under
the Creative Commons Attribution 3.0 License.

Annales Geophysicae

Convection: the likely source of the medium-scale gravity waves observed in the OH airglow layer near Brasilia, Brazil, during the SpreadFEx campaign

S. L. Vadas[1], M. J. Taylor[2], P.-D. Pautet[2], P. A. Stamus[1], D. C. Fritts[1], H.-L. Liu[3], F. T. São Sabbas[4], V. T. Rampinelli[4], P. Batista[4], and H. Takahashi[4]

[1]NorthWest Research Associates, CoRA div., 3380 Mitchell Lane, Boulder, CO, USA
[2]Center for Atmospheric and Space Sciences, Utah State University, Logan, USA
[3]High Altitude Observatory, NCAR, Boulder, CO, USA
[4]Instituto Nacional de Pesquisas Espaciais, INPE, Sao Jose dos Campos, SP, Brazil

Received: 4 April 2008 – Revised: 14 November 2008 – Accepted: 18 November 2008 – Published: 14 January 2009

Abstract. Six medium-scale gravity waves (GWs) with horizontal wavelengths of λ_H=60–160 km were detected on four nights by Taylor et al. (2009) in the OH airglow layer near Brasilia, at 15° S, 47° W, during the Spread F Experiment (SpreadFEx) in Brazil in 2005. We reverse and forward ray trace these GWs to the tropopause and into the thermosphere using a ray trace model which includes thermospheric dissipation. We identify the convective plumes, convective clusters, and convective regions which may have generated these GWs. We find that deep convection is the highly likely source of four of these GWs. We pinpoint the specific deep convective plumes which likely excited two of these GWs on the nights of 30 September and 1 October. On these nights, the source location/time uncertainties were small and deep convection was sporadic near the modeled source locations. We locate the regions containing deep convective plumes and clusters which likely excited the other two GWs. The last 2 GWs were probably also excited from deep convection; however, they must have been ducted ∼500–700 km if so. Two of the GWs were likely downwards-propagating initially (after which they reflected upwards from the Earth's surface), while one of the GWs was likely upwards-propagating initially from the convective plume/cluster. We also estimate the amplitudes and vertical scales of these waves at the tropopause, and compare their scales with those from a simple, linear convection model. Finally, we calculate each GW's dissipation altitude, location, and amplitude. We find that the dissipation altitude depends sensitively on the winds at and above the OH layer. We also find that several of these GWs may have penetrated to high enough altitudes to potentially seed equatorial spread F (ESF) if located somewhat farther from the magnetic equator.

Keywords. Atmospheric composition and structure (Airglow and aurora; General or miscellaneous)

1 Introduction

Gravity waves (GWs) can be excited by convection, wind flow over mountains, geostrophic adjustment, and wave breaking (e.g., Fritts and Alexander, 2003). The propagation angle from the horizontal plane for an upward-propagating GW is approximately the ratio of its vertical to its horizontal wavelength; as this ratio increases, this propagation angle increases, with higher-frequency GWs propagating closer to vertical, and lower-frequency GWs propagating closer to horizontal (Hines, 1967). Since this ratio also approximates the GW frequency divided by the buoyancy frequency, the highest frequency waves propagate close to the zenith, while the lowest frequency waves propagate nearly horizontally. Additionally, the vertical group velocity of a wave is approximately proportional to its frequency times its vertical wavelength; for a fixed frequency, the larger the GW's vertical wavelength, the faster it can propagate to the mesopause and lower thermosphere (MLT), assuming it avoids critical levels and evanescence.

Correspondence to: S. L. Vadas
(vasha@cora.nwra.com)

Published by Copernicus Publications on behalf of the European Geosciences Union.

The naturally occurring nightglow emissions provide an important capability for remote measurements of gravity waves in the vicinity of the mesopause. Most imaging studies have used the bright near infrared hydroxyl OH emission which originates from a well defined layer centered at ∼87 km with a typical half-width of ∼8 km (Baker and Stair 1988). As a GW propagates through this layer, it modulates the line-of-sight brightness and rotational temperature of the airglow emission, which appears as coherent wave structure in sensitive all-sky imaging systems (e.g. Swenson and Mende, 1994; Taylor et al., 1995; Smith et al., 2000; Ejiri et al., 2003; Medeiros et al., 2003; Nielsen et al., 2006). Most of the time the waves appear near linear; however on occasions well-defined concentric rings of GWs are detected over or near severe thunderstorms (Taylor and Hapgood, 1988; Dewan et al., 1998; Sentman et al., 2003; Suzuki et al., 2007; Yue et al., 2008). Although Taylor and Hapgood (1988) inferred that a thunderstorm created the partial concentric rings which they observed, Sentman et al. (2003) showed that the concentric rings they observed originated from a severe thunderstorm. Yue et al. (2008) recently examined 9 cases of partial or full concentric rings caused by deep convection near Fort Collins, CO, during 5 years of observations.

Typically, the GWs measured by all-sky imagers have relatively small horizontal wavelengths (<50 km), observed horizontal phase speeds of a few 10s of meters/second, and short observed periods (typically 0–25 min) near the buoyancy period (Taylor et al., 1997; Nakamura et al., 1999; Hecht et al., 2001; Ejiri et al., 2003; Medeiros et al., 2003). While many are clearly freely propagating, a significant number of the GWs are thought to be ducted (or evanescent) in nature, particularly those having short horizontal wavelengths (Isler et al., 1997; Walterscheid et al., 1999; Hecht et al., 2001, 2004; Pautet et al., 2005; Snively et al., 2007). These GWs may have been excited directly from tropospheric sources; however, they may also have been excited from wave-wave or wave-mean flow interactions accompanying the breaking of GWs from wind flow over mountains and convection (e.g. Fritts and Alexander, 2003, and references therein). Because of their uncertain origins, and because of their small phase speeds, it is more difficult to utilize them via reverse ray tracing studies for source identification and quantification if there are large uncertainties in the horizontal winds. However, one study did determine, via reverse ray trace studies, that the small-scale GWs observed in the OH layer were probably excited from deep convection (Hecht et al., 2004).

On the other hand, the propagation paths of convectively-generated, high-frequency GWs with medium-scale horizontal wavelengths are much less sensitive to uncertainties in the horizontal winds in MLT, because their horizontal phase speeds are larger than for small-scale GWs. Since the useful field of view of all-sky measurements is typically 600 km at the OH emission height, GWs with medium-scale horizontal wavelengths of $\lambda_H \sim 60-500$ km can also be detected at the same time as the shorter-scale waves which tend to dominate the image structure. Such measurements are usually also accompanied by background images to account for any contamination by meteorological clouds. Medium-scale GWs with brightness amplitudes of several percent are easily detected in the OH layer. These waves are generally believed to be excited at or near the tropopause or lower stratosphere from processes such as convection, air flow over mountains, and geostrophic adjustment, rather than from wave breaking near the mesopause, which mostly creates small-scale, secondary GWs (e.g. Fritts and Alexander, 2003). Note that medium-scale, secondary GWs are excited near the mesopause from the localized deposition of momentum which occurs during wave-breaking (Vadas et al., 2003); however, the amplitudes of these waves are only a few percent of the original breaking wave's amplitude, and are therefore less-likely to be detected in the OH layer. When there are significant wind uncertainties, reverse ray tracing medium-scale GWs from the OH layer likely yields a more accurate identification and quantification of their sources than reverse ray tracing small-scale GWs from the OH layer, because their phase speeds tend to be larger in general. However, a significant drawback is that medium-scale GWs are much less frequently observed than small scale GWs.

Recently, Taylor et al. (2009) observed and measured the wavelengths, periods, and phase speeds of six medium-scale GWs with $\lambda_H = 60-160$ km in the OH airglow layer near Brasilia, Brazil, during the SpreadFEx in September–November 2005. These observations provided key data in relatively close proximity to expected convective sources of the GWs (located primarily to the West over the state of Mato Grosso). However, they were often constrained by local thunderstorm activity during the latter part of the second observing period. In this paper, we reverse and forward ray trace these six GWs in order to identify and quantify their sources, and to estimate their dissipation altitudes, locations, and times in the thermosphere. Our paper is structured as follows. In Sect. 2, we provide a brief description of the ray trace model, and the wind and temperature models. In Sect. 3, we briefly review the characteristics of these six GWs. In Sect. 4, we reverse ray trace these GWs from the OH layer to the tropopause. We include ground reflection here, and so model both tropospheric source locations and times from which the GW may have been excited. We also show the results of forward ray tracing these GWs upwards into the thermosphere. Section 5 compares the computed source locations and times with deep convection from satellite images. Section 6 provides the amplitudes of these GWs in the OH layer, and compares them with the amplitudes of GWs excited from a simple convection model. Our conclusions are provided in Sect. 7.

2 Methodology

In this section, we describe the methods we use to determine the likely tropospheric sources of the observed GWs, and to determine their penetration to higher altitudes in the thermosphere.

2.1 Ray trace model

Ray tracing has been used for decades for geophysical problems of interest (e.g. Jones, 1969; Marks and Eckermann, 1995; Cowling et al., 1971; Waldock and Jones, 1984, 1987; Hung and Kuo, 1978; Hung and Smith, 1978; Lighthill, 1978; Gerrard et al., 2004; Hecht et al., 2004; Wrasse et al., 2009; Lin and Zhang, 2008). Although these past formalisms allowed for the propagation of GWs through varying 3-D winds and temperatures, they did not allow for the propagation of high-frequency GWs through a thermosphere containing realistic dissipation. Recently, an anelastic dispersion relation was derived which improves upon past ray trace models by taking into account the effects of kinematic viscosity and thermal diffusivity in the thermosphere for high-frequency GWs (Vadas and Fritts, 2005). This dispersion relation is

$$m^2 = \frac{k_H^2 N^2}{\omega_{Ir}^2(1+\delta_+ + \delta^2/\,\mathrm{Pr})} \left[1 + \frac{\nu^2}{4\omega_{Ir}^2}\left(\mathbf{k}^2 - \frac{1}{4\mathrm{H}^2}\right)^2 \frac{(1-\mathrm{Pr}^{-1})^2}{(1+\delta_+/2)^2}\right]^{-1} - k_H^2 - \frac{1}{4\mathrm{H}^2}, \quad (1)$$

where $\mathbf{k}=(k,l,m)$ is the GW zonal, meridional, and vertical wavenumber components in geographic coordinates, respectively,

$$\lambda_x = 2\pi/k, \qquad \lambda_y = 2\pi/l, \qquad \lambda_z = 2\pi/m \quad (2)$$

are the zonal, meridional, and vertical wavelengths, respectively, $k_H^2=k^2+l^2$, $\mathbf{k}^2=k_H^2+m^2$, N is the buoyancy frequency, Pr is the Prandtl number, μ is the viscosity coefficient, $\nu=\mu/\overline{\rho}$ is the kinematic viscosity, $\kappa=\nu/\,\mathrm{Pr}$ is the thermal diffusivity, $\overline{\rho}$ is the mean density, $\mathrm{H}=-\overline{\rho}(d\overline{\rho}/dz)^{-1}$ is the density scale height,

$$\omega_{Ir} = \omega_r - k\,U - l\,V \quad (3)$$

is the intrinsic frequency (in a frame moving with the wind), ω_r is the observed frequency, U and V are the zonal and meridional winds, respectively, $\delta=\nu m/\mathrm{H}\omega_{Ir}$, and $\delta_+=\delta(1+\mathrm{Pr}^{-1})$. At altitudes where thermospheric dissipation is negligible ($z<110$ km), Eq. (1) reduces to the usual anelastic, dissipativeless dispersion relation when the Earth's rotation can be neglected (Marks and Eckermann, 1995):

$$\omega_{Ir}^2 = \frac{k_H^2 N^2}{m^2 + k_H^2 + 1/4\mathrm{H}^2}. \quad (4)$$

Additionally, assuming negligible wave reflection from viscosity, which can cause a GW to partially reflect downwards as it continues to propagate upwards (Midgley and Lieholm, 1966; Yanowitch, 1967; Volland, 1969), a GW's amplitude grows in altitude as $\propto 1/\sqrt{\overline{\rho}}$, but decays in time from dissipation as $\exp(\omega_{Ii}\,t)$, where ω_{Ii} is the dissipative decay rate (Vadas and Fritts, 2005):

$$\omega_{Ii} = -\frac{\nu}{2}\left(\mathbf{k}^2 - \frac{1}{4\mathrm{H}^2}\right)\frac{[1+(1+2\delta)/\,\mathrm{Pr}]}{(1+\delta_+/2)}. \quad (5)$$

Although this dispersion relation is not important below the turbopause at $z\sim$110 km, it is very important above the turbopause, where dissipation is the primary mechanism for damping high-frequency GWs.

Here, we briefly describe the inputs and outputs of the ray trace model developed with this dissipative dispersion relation. A full description of this dissipative ray trace model is given in Vadas and Fritts (2009). Consider a GW observed in the OH airglow layer with ground-based frequency ω_r and wavenumber vector $\mathbf{k}=(k,l,m)$. In order to ray trace this GW forwards and backwards in time from the airglow layer, the background winds and temperatures, $\overline{T}$, are needed as a function of horizontal location, altitude, and time. If the winds vary with altitude, the GW's intrinsic frequency changes with altitude. We assume that the GW's ground-based frequency is constant along its ray path; this is only strictly true if the background winds and temperatures do not vary in time (Jones, 1969). The intrinsic frequency allows for the determination of the GW's vertical wavelength and vertical group velocity from the dispersion relation. We input the GW's amplitude, k, l, m, ω_r, along with the background arrays U, V, and $\overline{T}$, into the ray trace model at a given location and time. The model then ray traces the GW backwards and forwards in time, and outputs its amplitude and wavenumber as a function of x, y, z, and t, where x, y, and z are the geographic zonal, meridional and vertical coordinates, and t is time.

2.2 Temperature and wind models

The temperature and wind models we use here depend on x, y, z, and t. Below ~25–30 km, we use the temperature and wind data analyzed from balloon soundings using the WXP analysis package. The temperature model used here for $z>35$ km is the Thermosphere-Ionosphere-Mesosphere-Electrodynamics General Circulation Model (TIME-GCM) (Roble and Ridley, 1994). The wind model above 35 km implements a combination of TIME-GCM model data and meteor radar data averaged from 2 sites in Brazil, at Cariri and Cachoeira Paulista (see below). We utilize TIME-GCM horizontal winds from 35 km to 70 km, meteor radar horizontal winds from 80 to 100 km, and TIME-GCM horizontal winds from 110 km to 350 km. For altitudes between these different data/model sets, we obtain the horizontal winds via linear interpolation.

The TIME-GCM data we use here extends from 35 km to 350 km altitude with a resolution of 2 grids/scale height and $5^\circ \times 5^\circ$ horizontally. The model includes all of the important aeronomical processes appropriate for these regions as described by Roble and Ridley (1994) and Roble (1995). The TIME-GCM is forced at the lower boundary by the NCEP reanalysis data. The gravity wave forcing in this model is parameterized, and is based on linear saturation theory (Lindzen, 1981; Boville, 1995). Thermospheric tides come from both in-situ diabatic heating and the upward propagation of large-scale waves from the lower atmosphere. These tides cause large perturbations in the temperatures and winds in the thermosphere. The dominating tidal modes in the thermosphere are migrating diurnal and semi-diurnal tides, with the latter dominating in the lower thermosphere and the former dominating at higher altitudes (Forbes, 1995).

Among other quantities, the TIME-GCM outputs U, V, the temperature $\overline{T}$, mean density $\overline{\rho}$, horizontal winds, and the mass mixing ratio of O and O_2, $\mathrm{mmr_O}$ and $\mathrm{mmr_{O_2}}$, respectively, as functions of (x, y, z, t). Here, the mass mixing ratio is the mass of the substance contained within a unit mass of the entire fluid. Since the atmosphere is composed mainly of 3 species, N_2, O and O_2, $(\mathrm{mmr_{N_2}}+\mathrm{mmr_{O_2}}+\mathrm{mmr_O})$=1. The mean molecular weight is then

$$\mathrm{X_{MW}} = \frac{1}{\mathrm{mmr_O}/16 + \mathrm{mmr_{O_2}}/32 + \mathrm{mmr_{N_2}}/28}. \quad (6)$$

From these quantities, we obtain the mean specific heats at constant pressure and constant volume, C_p and C_v, respectively, via

$$C_p = R\mathrm{X_{MW}}^2 \left[\left(1+\frac{5}{2}\right)\left(\frac{\mathrm{mmr_{N_2}}}{28^2}+\frac{\mathrm{mmr_{O_2}}}{32^2}\right) + \left(1+\frac{3}{2}\right)\frac{\mathrm{mmr_O}}{16^2}\right] \quad (7)$$

$$C_v = R\mathrm{X_{MW}}^2 \left[\frac{5}{2}\left(\frac{\mathrm{mmr_{N_2}}}{28^2}+\frac{\mathrm{mmr_{O_2}}}{32^2}\right) + \frac{3}{2}\frac{\mathrm{mmr_O}}{16^2}\right], \quad (8)$$

where the universal gas constant is R=8314.5/$\mathrm{X_{MW}}$ $\mathrm{m^2\,s^{-2}\,K^{-1}}$. Then the ratio of specific heats is $\gamma = C_p/C_v$. The molecular weight $\mathrm{X_{MW}}$ decreases from 29 to 16 and γ increases from 1.4 to 1.7 in the thermosphere because of the the change in composition from primarily diatomic N_2 and O_2 to monotomic O. Below 35 km we set γ=1.4 and $\mathrm{X_{MW}}$=29. We interpolate U, V, $\overline{T}$, $\overline{\rho}$, $\mathrm{X_{MW}}$, and γ, onto the ray trace grid we use here. Then, we determine the background pressure via the ideal gas law, $\overline{p} = R\overline{\rho}\overline{T}$. In addition, the potential temperature is $\overline{\theta} = \overline{T}(p_s/\overline{p})^{R/C_p}$, the standard pressure at sea level is p_s, the buoyancy frequency is $N = \sqrt{(g/\overline{\theta})\, d\overline{\theta}/dz}$, and the coefficient of molecular viscosity is

$$\mu = 3.34 \times 10^{-4} \overline{T}^{0.71}\ \mathrm{gm\,m^{-1}\,s^{-1}} \quad (9)$$

(Dalgarno and Smith, 1962). Here, we set the Prandtl number to be Pr = 0.7 (Kundu, 1990), and thus ignore its slight variations with temperature (Yeh et al., 1975).

Meteor radar data was obtained at 2 sites in Brazil during this experiment to determine the zonal and meridional horizontal winds from z=80−100 km. Here, the sites were Cariri (São João do Cariri) located at 7.4° S, 36.5° W, and Cachoeira Paulista, located at 22.7° S, 45.0° W (Batista et al., 2004; Buriti et al., 2008). The equipment used to observe winds in the mesosphere at Cariri and at Cachoeira Paulista are similar to the SKiYMET All-Sky Interferometric Meteor Radar which uses an antenna array composed of 2-element yagi antennas (5 in total) for reception, and a 3-element yagi transmitting antenna. These particular SKiYMET operate at a frequency of 35.24 MHz, and have an output power of 12 KW peak. The radar measures the radial velocity by transmitted radiation scattered from meteors trails. The differences of phase of the signal received by each possible pairing of antennas permits the determination of the location of the trail. The range is obtained by the delay between the transmitted and received signals. Zonal, meridional, and vertical velocity components are then determined by a least mean squares fit to all of the radial velocities measured in a given time/height bin. The radars typically provide around 3000–5000 useful echoes per day. Vertical velocities are normally very small and are ignored here. The temporal and vertical resolutions used here are 1 h and 3 km. The altitudes are centered at z=81, 84, 87, 90, 93, 96, and 99 km, respectively. Technical and acquisition details about this radar can be found in Hocking et al. (2001).

Figure 1 shows the locations of the OH all-sky imager at Brasilia (BR) and the meteor radars at Cariri (CA) and Cachoeira Paulista (CP) in Brazil. Other instrument sites for the SpreadFEx are described in Fritts et al. (2009).

Figure 2 shows the meteor radar winds at z=87 km at CA (upper two rows) and at CP (lower two rows) for days 270–300 in 2005. Day 272 is 30 September (the first day a medium-scale GW was observed), while day 296 is 24 October (the last day a medium-scale GW was observed). Although the winds are highly variable, diurnal and semidiurnal variations are easily seen.

Figure 3 shows altitude profiles of the meteor radar zonal and meridional winds at CA (upper row) and CP (lower row) at 23:00 UT on 1 October 2005. This is a night when strong convection was occurring west and southwest of Brasilia. We see that the meridional winds are much larger at CP than at CA. Additionally, the zonal winds have disimilar altitude profiles.

Figure 4 shows the full temperature and wind models on the same evening, 1 October 2005. The upper row shows the models at 52.5° W and 15° S at 21:00 UT (solid lines) and 23:00 UT (dash lines). The lower row shows the models at 47.5° W and 15° S at 23:00 UT (solid lines) and 24:00 UT (dash lines). We see that the horizontal winds vary spatially and temporally reasonably significantly, especially for

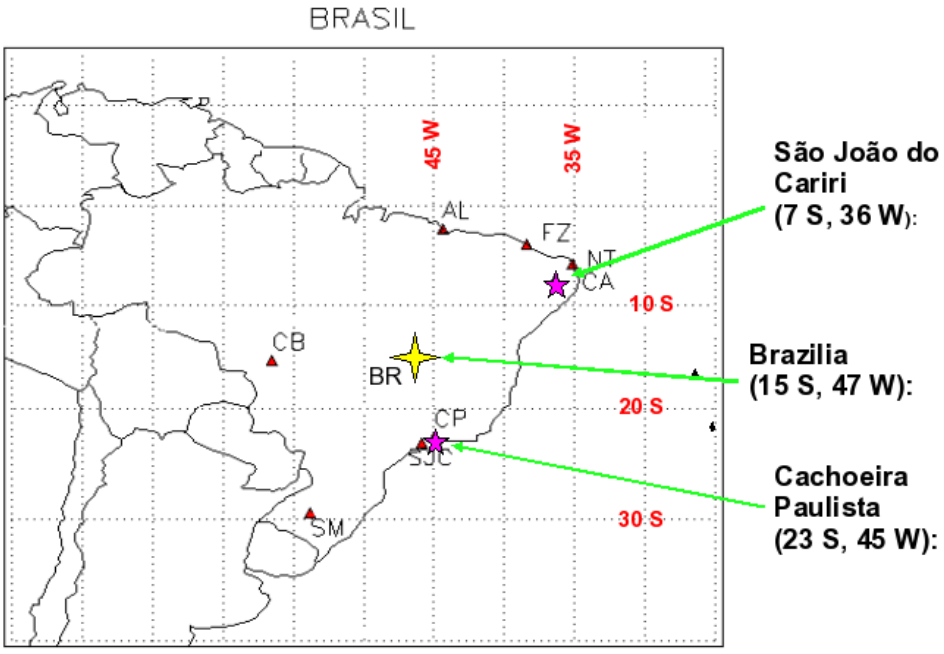

Fig. 1. Approximate locations in Brazil of the all-sky imager at Brasilia (BR) (yellow star), and the meteor radars at Cariri (CA) and Cachoeira Paulista (CP) (purple stars).

$z>100$ km. At the highest altitudes, the diurnal tide is the dominant contributor to the background horizontal wind. The spatial and temporal variations in the temperatures, however, are quite small.

Because these model winds are somewhat uncertain, we also ray trace the GWs through zero winds in order to assess the dependence of our results on the winds. We initialize each GW at z=87 km at the appropriate time and location, and reverse ray trace it through each of these two winds back to the tropopause. We then forward ray trace each GW upwards from z=87 km through each of these two winds until it reflects, dissipates, or meets a critical level. By varying the winds, we better understand the uncertainties associated with the estimated 1) source time and location, and 2) dissipation altitude, location, and time.

3 Medium-scale gravity waves in the OH airglow layer

The USU all-sky imager was deployed near Brasilia, Brazil, at -47.603^o longitude and -14.754^o latitude. This imager utilized a Photometrics CH250 camera fitted with a sensitive back-thinned 1024×1024 pixel charge couple device (CCD). A computer controlled filter wheel enabled sequential measurements of selected airglow emissions: the mesospheric near infra red (NIR) hydroxyl (OH) Meinel broad band emission (710–930 nm) and the OI (630.0 nm) thermospheric redline emission, which originate from layers centered at $z\sim87$ and $z\sim250$ km, respectively. The data were 2×2 binned on chip down to 512 by 512 pixels, providing a zenith horizontal resolution of ∼0.5 km (e.g. Taylor et al., 1995). Exposure times were 15 s for the OH data and 120 s for the OI (630.0 nm) data, giving a 2.5 min acquisition cycle. Further details on the instrument and the airglow measurements performed in Brazil during this experiment are given in Taylor et al. (2009).

In Table 1, we list the ground-based (i.e. observed) characteristics of the six medium-scale GWs with $\lambda_H>60$ km that were observed with this all-sky imager (near Brasilia) in the OH airglow layer during the SpreadFEx. These GWs were observed during four nights of the experiment. From left to right, the columns display the date (in 2005), the start time (in UT), the duration (hrs:min), the propagation angle θ in the horizontal direction clockwise from north (in degrees), the horizontal wavelength λ_H (in km), the observed horizontal phase speed $c_H=\omega_r/k_H$ (in m/s), the observed wave period $2\pi/\omega_r$ (in min), and the relative intensity of the perturbation $I'/\bar{I}$ (in %). Note that the horizontal wavelengths range from 60–160 km, and the horizontal phase speeds range from 25−75 m/s. As an example, the GW with λ_H=158.6 km is shown in Fig. 2b in Taylor et al. (2009). Note that θ=90^o if the wave is propagating eastward. Although GWs with horizontal wavelengths greater than 100 km can penetrate above the turbopause, they must typically have intrinsic phase speeds greater than $c_{IH}>100$ m/s to propagate to the bottomside of the F-region (Vadas, 2007). Using Eq. (3), the intrinsic and observed horizontal phase speeds are related via a Doppler shift from the moving to the ground-based frame of reference:

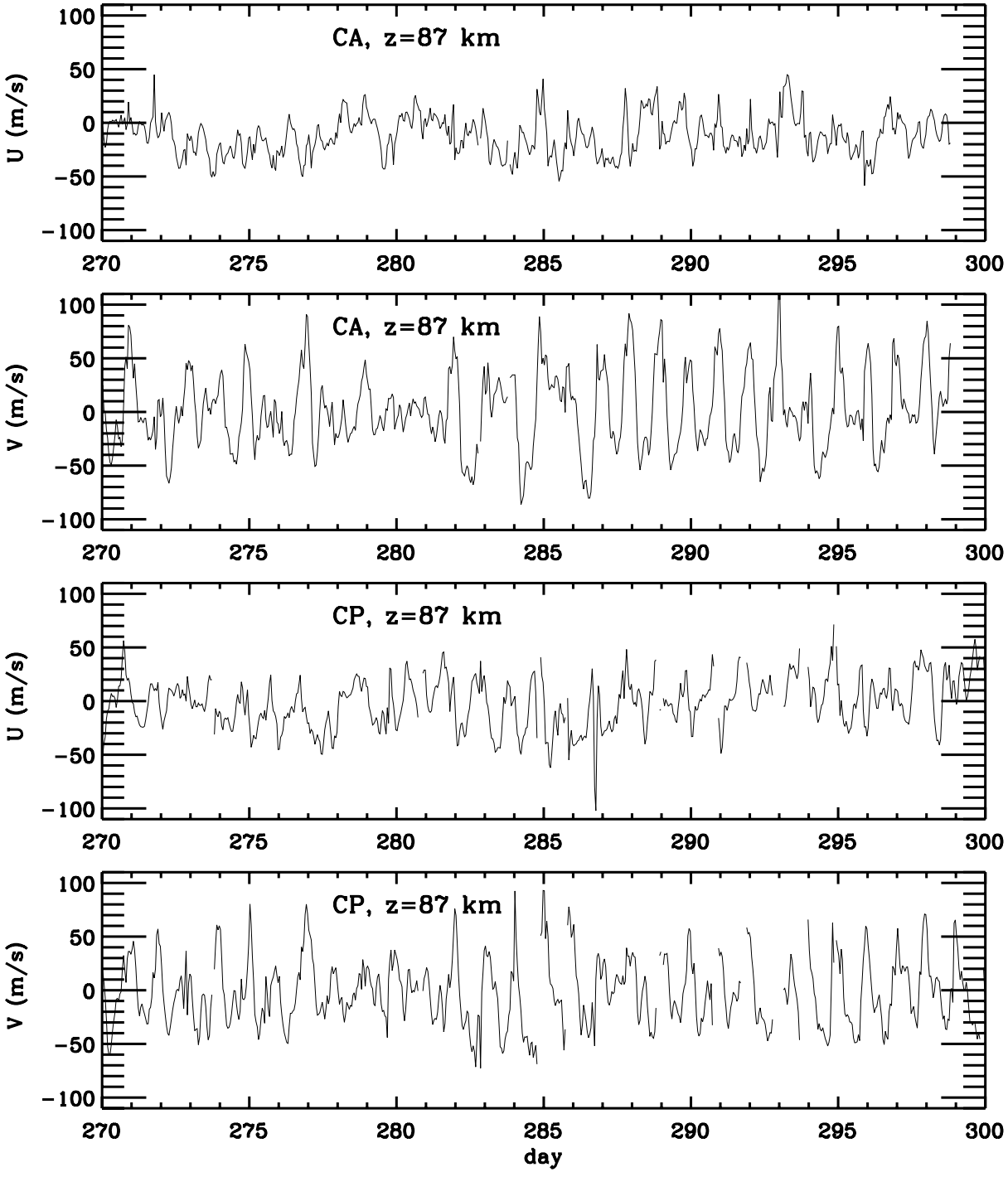

Fig. 2. Zonal and meridional meteor radar winds at CA (upper two rows) and at CP (lower two rows), as labeled, as a function of day number, at z=87 km. These data encompass the time period in 2005 for which the 6 medium-scale GWs were observed in the OH layer near Brasilia.

$$c_{IH} = c_H - U_H, \tag{10}$$

where U_H=(k U+l V)/k_H is the component of the wind along the direction of GW propagation. Although the horizontal scales of these observed medium-scale GWs are ideal, these GWs do not have large enough horizontal phase speeds to penetrate to the bottomside of the F-region, unless the background thermospheric winds are large enough (i.e. $>$50 m/s) and are in a direction opposite to the GW's propagation direction (Fritts and Vadas, 2008).

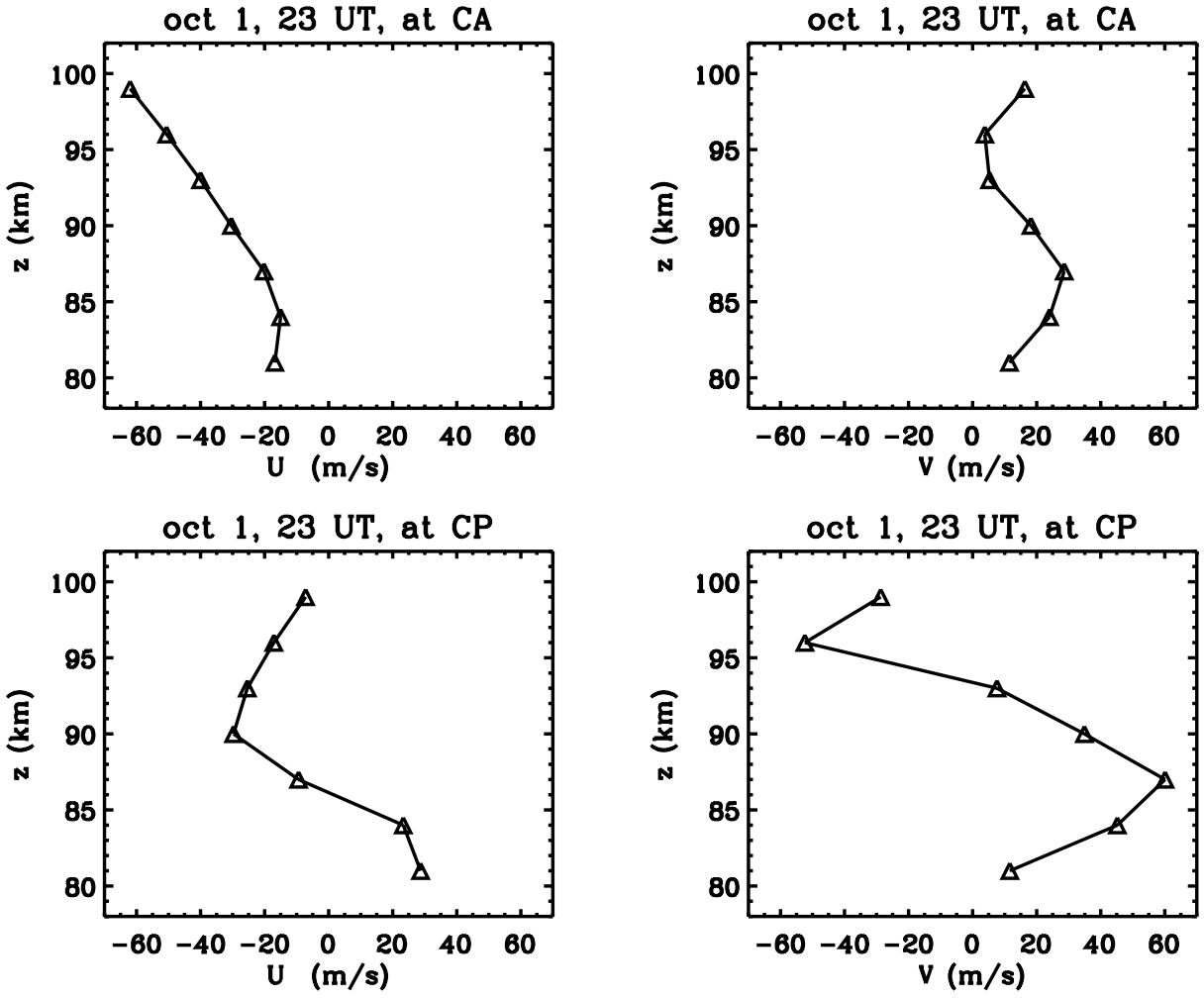

Fig. 3. Meteor radar winds at CA (upper row) and CP (lower row) on 1 October 2005, at 23:00 UT. The zonal and meridional winds are shown in the left and right columns, respectively.

Table 1. Measured medium-scale gravity wave events near Brasilia.

Date	Start Time	Duration	θ	λ_H (km)	c_H (m/s)	$2\pi/\omega_r$ (min)	$I'/\overline{I}$
30 Sep–1 Oct	02:39	1:00	84.3^o	145.1	71.3	33.9	3.8
1–2 Oct	23:06	2:45	90.0^o	71.4	57.8	20.6	3
1–2 Oct	01:03	3:45	96.8^o	158.6	50.2	52.7	7
22–23 Oct	00:31	0:55	145.9^o	64.0	70.2	15.2	2
23–24 Oct	23:54	3:15	143.4^o	61.4	28.7	35.7	3.1
23–24 Oct	01:36	1:05	136.3^o	148.3	27.4	90.2	2.9

Figure 5 shows satellite images on the 4 nights these GWs were observed. These images show brightness temperatures (equivalent blackbody temperature) in the infrared (IR) band, which is a surrogate for (but does not equal) the actual temperature (see, e.g. Menzel and Purdom, 1994, and references within). Light blue shading indicates regions where colder cloud material is located near the tropopause. Localized dark blue shading denotes regions with the coldest brightness temperatures, indicative of regions of active convection. The image times are noted in UT, and the conversion to local time (LT) is LT=UT−3. We show the approximate location of the all-sky imager as a yellow dot, and the approximate

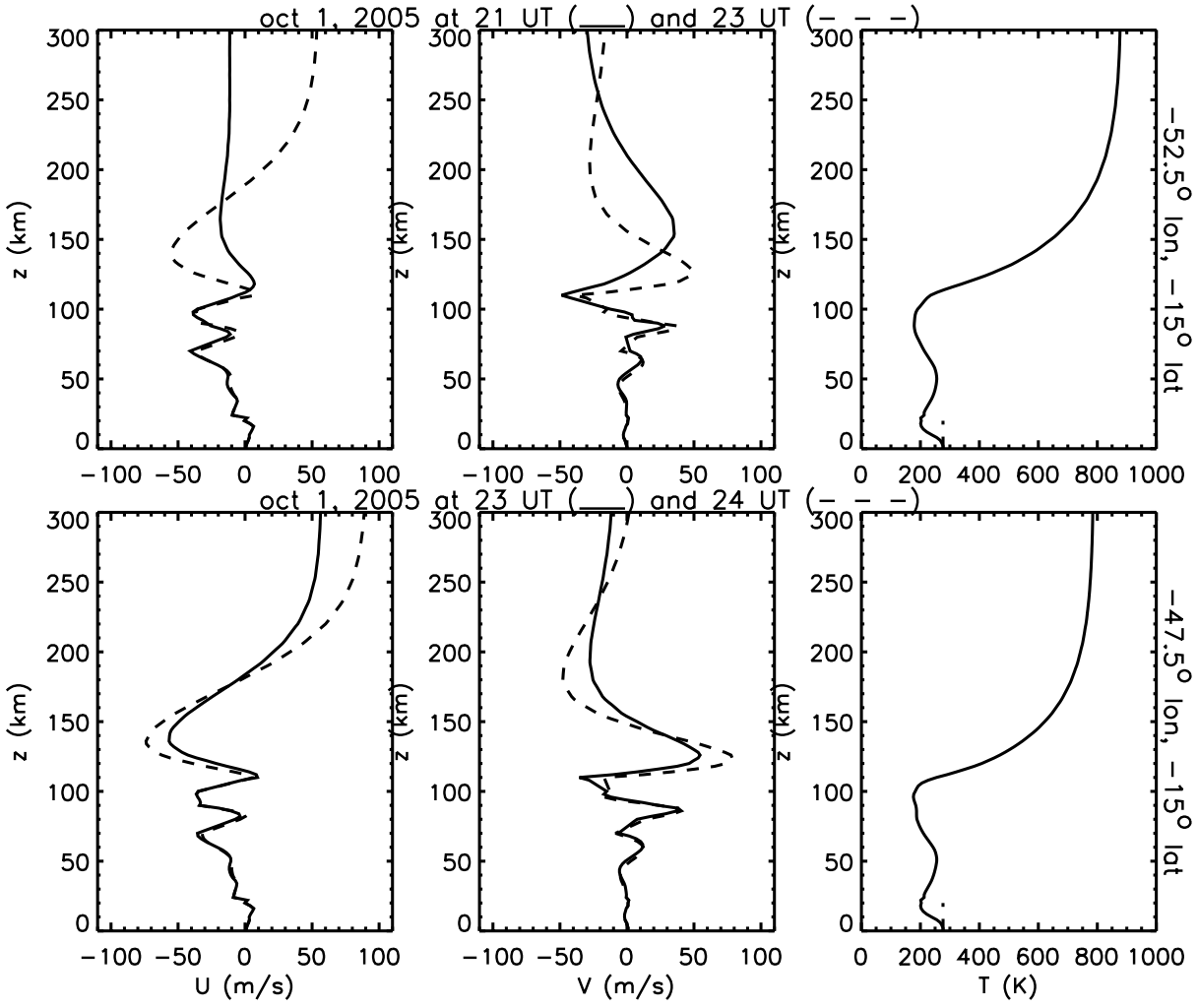

Fig. 4. Zonal wind model, meridional wind model and temperature model in the first, second, and third columns, respectively, on 1 October 2005. The first row shows the results at -52.5^{o} longitude and -15.0^{o} latitude at 21:00 UT (solid lines) and 23:00 UT (dash lines). The second row shows the results at -47.5^{o} longitude and -15.0^{o} latitude at 23:00 UT (solid lines) and 24 UT (dash lines).

propagation directions of the observed medium-scale GWs from Table 1 with red arrows.

At the end of September and the beginning of October, active convective regions are isolated, and the nearest regions of strong, active convection are west, northwest, and southwest of the all-sky imager near Brasilia. Near the end of October, however, active convection is more organized and widespread, and the nearest regions of active, strong convection are west and northwest of the all-sky imager. Because these directions correspond to the directions these medium-scale GWs propagated from, Fig. 5 suggests that these GWs may have been excited by convection. As further evidence of this hypothesis, Taylor et al. (2009) reports that the short-wavelength GWs observed in the OH layer propagated southeastward during the first observing period from 22 September–9 October, and propagated eastward during the second observing phase from 22 October–9 November). Thus, the observed short-wavelength GWs also propagated from the general direction that active convection occurred. Importantly, there is no active convection occurring on these nights to the south, southeast, east, and northeast of the all-sky imager, and none of the observed small or medium-scale GWs were observed propagating from these directions (Taylor et al., 2009). Additionally, these medium-scale GWs could not have been excited by air flow over mountains, because their horizontal phase speeds are much greater than zero. Since they are high-frequency waves, they are also unlikely to have been excited by geostrophic adjustment. Another potential source of medium-scale GWs is the deposition of momentum which occurs during wave-breaking near the mesopause (Vadas et al., 2003). However, the amplitudes of these medium-scale, secondary GWs are only a few percent of the primary breaking GW, and are therefore less-likely to be detected in the OH airglow layer. (Wave breaking

also excites large-amplitude GWs, but with small horizontal scales (e.g. Fritts and Alexander, 2003).)

This figure strongly suggests that these observed, medium-scale GWs were likely created by deep convection. We will explore this conjecture in the following section via reverse ray trace studies. Although many of the small-scale GWs observed by Taylor et al. (2009) may have been excited by convection, because of their smaller phase speeds and enhanced sensitivity to uncertainties in the horizontal winds in the OH layer, they are less useful for source identification and quantification via reverse ray tracing. We will therefore only reverse ray trace the observed medium-scale GWs here.

4 Ray tracing medium-scale gravity waves

4.1 Intrinsic parameters of medium-scale GWs

We begin by initializing each GW from Table 1 at the start time t (from Table 1) and at the assumed altitude z=87 km. The flat field of view of the OH airglow layer is 500 km×500 km. We position each GW on a circle centered on the all-sky imager with radius 250 km, at the location that the GW propagated from:

$$x = x_B + (250 \text{ km}) \cos(\zeta) \quad (11)$$

$$y = y_B + (250 \text{ km}) \sin(\zeta), \quad (12)$$

where (x_B, y_B) is the location of the all-sky imager, and ζ=180+(90−θ) is the angle counterclockwise from east that the GW propagated from. We then choose the model wind or zero wind. The wind values and derived GW parameters are displayed in Table 2. For each GW, rows 1 and 2 display the results when the horizontal wind is zero and equals the model wind, respectively. The second row represents our "best guess", while the first row gives us an estimate of the sensitivity of our results to the model wind. The columns, from left to right, show the horizontal wavelength λ_H (in km), the start time t (in fractions of an hr), the zonal and meridional winds U and V, respectively, (in m s^{-1}), the zonal, meridional, and vertical wavelengths λ_x, λ_y, and λ_z, respectively, (in km), the intrinsic GW period $2\pi/\omega_{Ir}$ (in min), and the vertical group velocity $c_{g,z}$=$\partial\omega_{Ir}/\partial m$ (in m s^{-1}). Since the GW wavelengths are calculated using Eq. (2), their signs depend on the direction of propagation. Positive λ_x denotes that the GW is propagating eastward, and positive (negative) λ_y denotes that the GW is propagating northward (southward). Additionally, λ_z<0 denotes that the GW is propagating upwards.

Table 2 shows that different horizontal winds greatly affect a GW's parameters in the OH layer; in particular, λ_z and τ_{Ir} depend sensitively on the winds in the OH layer. Note that the GW with λ_H=148.3 km has the smallest vertical group velocity. Coupled with a relatively small horizontal phase speed of c_H=27.4 m/s (see Table 1), we will see in Sect. 4.4 that this GW dissipates near the turbopause at z∼110 km. Other medium-scale GWs have vertical group velocities up to $c_{g,z}$∼40 m/s, with corresponding horizontal phase velocities up to c_H=75 m/s. Having larger values of $c_{g,z}$ and c_H enables a GW to more easily avoid critical levels and propagate above the turbopause prior to dissipating, as we will see in Sect. 4.4. However, since λ_z and $c_{g,z}$ change with altitude and time as the winds change, their values at z=87 km are not equal to their values in the thermosphere; therefore, we cannot predict their penetration altitude in the thermosphere based on their values in the OH airglow layer.

4.2 Reverse ray tracing medium-scale gravity waves

We now ray trace each GW backwards in time from its initial location in the OH airglow layer to the tropopause, if critical levels are not encountered. Here, we assume the tropopause to be located at z∼16 km (São Sabbas et al., 2009). Critical levels occur when c_H=U_H, and cause the GW to dissipate rapidly (e.g. Fritts and Alexander, 2003). Because we are reverse ray tracing, encountering critical levels implies that 1) the model winds were not realistic, or 2) the wave was excited above this altitude. This is a common occurrence reverse ray tracing small-scale GWs from the OH layer. However, none of these medium-scale GWs encounter critical levels during reverse ray tracing. Ray tracing is performed in a numerical box with longitudes=[−80°, −30°], latitudes=[−22.5°, 2.5°], and z=[0, 400] km. The earliest time we reverse ray trace to on each day is 06:00 UT.

We also include the possibility that the medium-scale GW was initially downward-propagating, and reflected off the ground before propagating into the OH airglow layer. This was theorized to occur (Francis, 1974), and was later observed experimentally (e.g. Samson et al., 1990). The boundary condition we use here for GW reflection is 1) that the vertical velocity is zero at the Earth's surface, so that the GW propagation angle with respect to the zenith is the same prior to and directly after reflection, and 2) that the horizontal direction of propagation is preserved. Here, we consider 2 possibilities for each observed GW: 1) that it propagated upwards initially after being excited from a convective plume, and thereafter propagated directly to the OH layer, and 2) that it propagated downwards initially after being excited from a convective plume, reflected upwards at the Earth's surface, and thereafter propagated upwards to the OH layer. Note that the latter possibility leads to a modeled source that occurs earlier in time and is a larger distance from the all-sky imager. Thus we first determine the location and time where each GW reaches the tropopause the "second" time during reverse ray tracing (backwards in time). (This is the location closer to the imager). We then allow the GW to reflect off the ground (backwards in time), and determine the location and time at which it reaches the tropopause the "first" time (which is earlier in time and farther from the imager). Note that the wave amplitude of the GW in our ray trace model does not change upon reflection off the Earth's

Table 2. Parameters in the OH layer for medium-scale GWs.

λ_H (km)	t (hrs)	U (m/s)	V (m/s)	λ_x (km)	λ_y (km)	λ_z (km)	$2\pi/\omega_{Ir}$ (min)	$c_{g,z}$ (m/s)
145.1	26.6	0.0	0.0	146	1461	−23	34.	10.
		−8.3	−6.4			−27	30.	13.
71.40	23.1	0.0	0.0	71	∞	−18	21.	13.
		−19.	33.			−24	16.	21.
158.6	25.1	0.0	0.0	160	−1339	−15	53.	4.5
		−21.	31.			−23	35.	9.6
64.00	24.5	0.0	0.0	114	−77	−22	15.	20.
		7.8	55.			−44	9.6	40.
61.40	23.9	0.0	0.0	103	−76	−9	36.	3.9
		−26.	47.			−29	12.	28.
148.3	25.6	0.0	0.0	215	−205	−8	90.	1.5
		−15.	29.			−18	42.	6.8

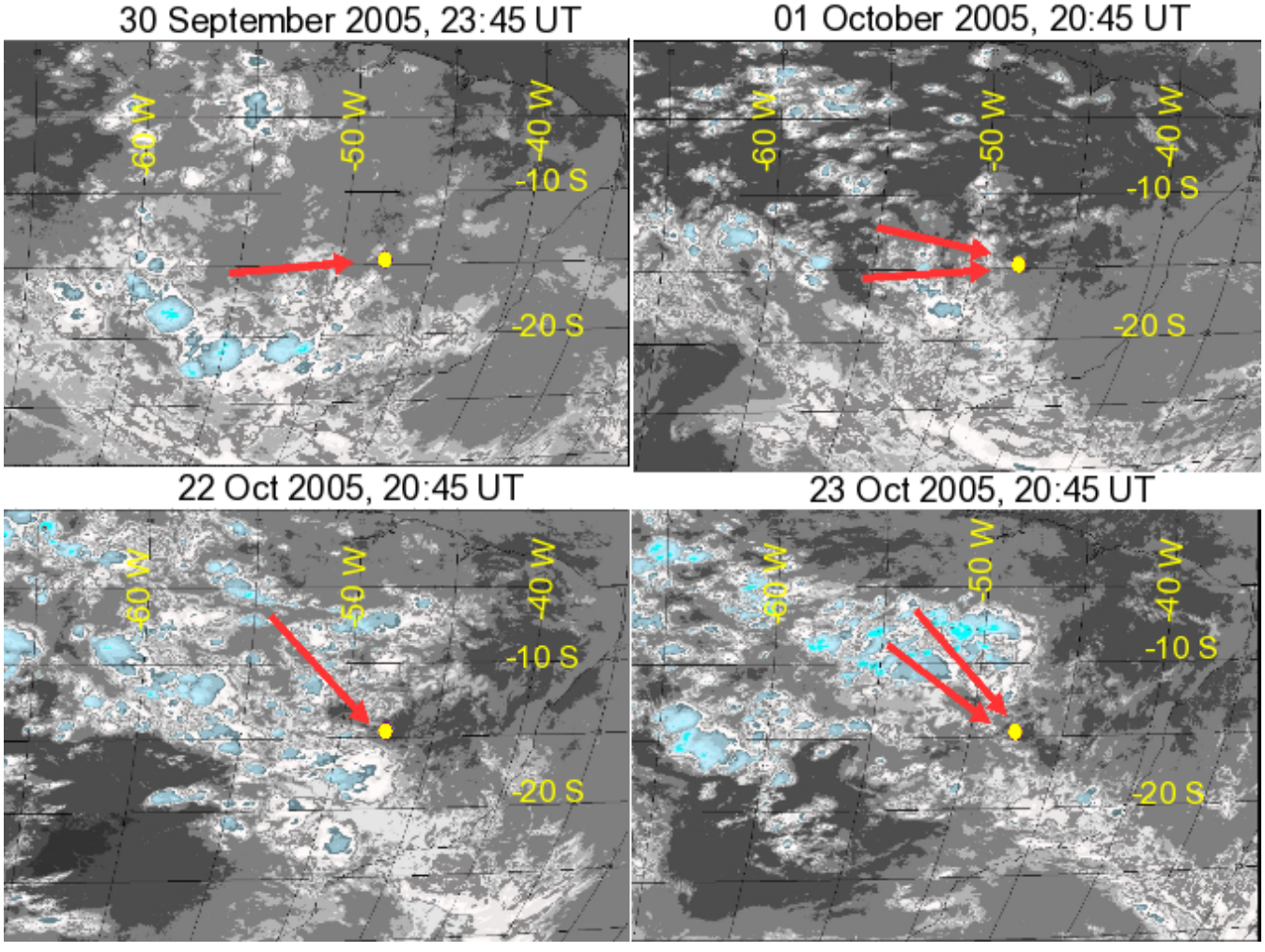

Fig. 5. Infrared satellite images showing convection over Brazil on 30 September at 23:45 UT (upper left), 1 October at 20:45 UT (upper right), 22 October at 20:45 UT (lower left), and 23 October at 20:45 UT (lower right). We also show the location of the all-sky imager near Brasilia (yellow dots), and the approximate direction of propagation of the six medium-scale GWs observed over Brasilia (red arrows).

surface, although it may decrease after reflection in nature. Figure 6 shows a sketch of these propagation paths from two convective plumes. The downward-propagating GW excited from source "1" reflects off the ground, then propagates upwards to the OH layer. The upward-propagating GW excited from source "2" propagates directly to the OH layer, and is observed by the all-sky imager at the same time and location as the GW from source "1". Thus source "1" is further away and earlier in time than source "2". By including the possibility that the observed GW reflected off the Earth's surface before propagating to the OH layer, we are allowing for a more realistic number of possible convective sources for this GW.

We show the results of reverse ray tracing in Table 3. For each GW, rows 1 and 2 display the results when the horizontal winds are zero and equal the model wind, respectively. The columns, from left to right, show the horizontal wavelength λ_H (in km), the average range (i.e. horizontal distance) of the source to the OH airglow location (in km), the average time taken to reach the source from the OH layer (in hours), the longitudes of each source (in deg), the latitudes of each source (in deg), the source times (in UT), the source altitudes (in km), the average $|\lambda_z|$ of the GW at the source (in km), and the ratio of the GW's momentum flux at the OH airglow layer to the average momentum flux at the tropopause. In columns 4–7, the first number shows the location or (later) time of source "2", and the second number shows the location or (earlier) time of source "1". If the tropopause is reached prior to reflection during reverse ray tracing, but not after reflection, then the source "1" altitude equals the altitude where ray tracing ended. (This occurs for the GW with λ_H=148.3 km in the model winds, because reverse ray tracing ended at 06:00 UT at z=10 km). Note that the entry in column 9 represents the ratio of momentum fluxes for a single GW. Since a GW packet disperses in volume as z^2 as it propagates upwards into the atmosphere, in order to estimate the GW spectral amplitudes from this ratio, one must divide this ratio by a factor which takes into account the increasing area within which the GW packet occupies (Fritts and Vadas, 2008).

There are several important results from Table 3. First, the difference in the source longitudes and latitudes between the zero and model winds is $(0.4-6)^o$ and $(0-3)^o$, respectively. Since 1^o is $\sim$110 km, and the diameters of typical convective plumes and clusters are 10–100 km across, it may not always be possible to pinpoint the particular convective plume or cluster which excited every GW; instead, we may only be able to identify regions of deep convection which excited some of the GWs. Second, the difference in the time to the tropospheric source, $\overline{\Delta t}$, is 0.2–3 h between the zero and model winds. Because typical convective plumes last less than an hour, we may not always be able to identify a particular convective plume or cluster which excited some of the GWs (although, again, we may be able to identify regions of deep convection). Although it may not always be possible to locate the precise convective plume or cluster which generated some of the GWs via reverse ray tracing, we can still gain some understanding of the characteristics of the convection which likely excited these GWs. During this experiment, active convection was often localized in the same area for many hours; during that time, the convective plumes had similar diameters and updraft velocities (see Sect. 5). Thus, it may not be necessary to know precisely which convective plume excited a GW; instead, determining the region and approximate time may allow for a reasonable understanding of the type of convection which likely excited a GW.

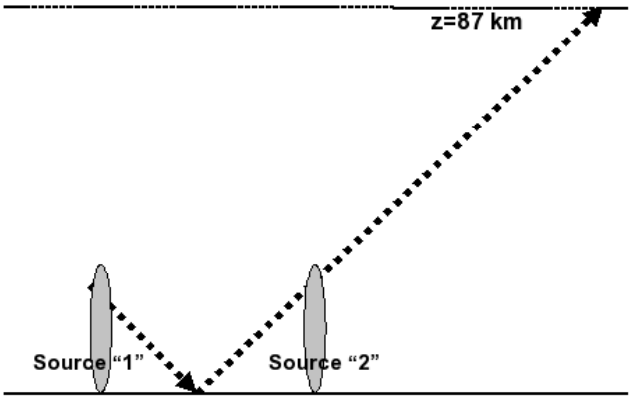

Fig. 6. Sketch showing how two convective plumes can excite GWs which reach the OH layer at the same time. Source "2" excites an upward-propagating GW which propagates to the OH layer along the thick dot line. Source "1" excites a downward-propagating GW earlier in time and farther from the imager; this GW reflects off the ground, then propagates upwards to the OH airglow layer along the same thick dot line. In this scenario, both GWs arrive at the OH layer at the same time, although they are from different convective plumes.

We see from Table 3 that the source range and time to source can be large or small depending of the characteristics of the GWs. Low-frequency GWs have a smaller ascent angle, and therefore travel further and take more time to reach the OH airglow layer than high-frequency GWs, which have steeper ascent angles closer to the zenith. For example, the low-frequency GW with λ_H=148.3 km is reverse ray traced to a source 900−1400 km from Brasilia, 15−18 h prior to its detection in the OH airglow layer. On the other hand, the high-frequency GW with λ_H=64 km is reverse ray traced to a source 140–220 km from Brasilia, 0.5–1.1 h prior to its detection in the OH airglow layer.

4.3 Forward ray tracing medium-scale gravity waves

As a GW propagates upwards in the thermosphere, as long as it avoids critical levels and evanescence, and as long as dissipation is unimportant, the GW's momentum flux increases nearly exponentially with altitude because the background density $\overline{\rho}$ decreases nearly exponentially with altitude. Since

Table 3. Reverse ray trace results for medium-scale gravity waves.

λ_H (km)	$\overline{\text{range}}$ (km)	$\overline{\Delta t}$ (h)	longitude of source	latitude of source	source time (UT)	z (km)	$\lvert\overline{\lambda_z}\rvert$ (km)	$\overline{u'_H w'_{87}}/\overline{u'_H w'_{16}}$
145.1	523	−1.9	−53.9, −55.1	−15.4, −15.5	24:58, 24:31	16, 16	27	4.1×10^4
	up*427	−1.7	−52.9, −54.4	−15.4, −15.5	25:16, 24:38	16, 16	23	4.1×10^4
71.40	dw*319	−1.7	−52.3, −53.1	−14.8, −14.8	21:41, 21:12	16, 16	20	4.0×10^4
	242	−1.3	−51.6, −52.4	−14.8, −14.8	22:02, 21:30	16, 16	18	4.2×10^4
158.6	*867	−5.2	−56.5, −58.6	−13.7, −13.5	20:41, 19:00	16, 16	15	4.1×10^4
	*618	−3.4	−54.2, −56.5	−14.0, −13.6	22:23, 20:52	16, 16	14	4.0×10^4
64.00	*221	−1.1	−49.9, −50.0	−11.3, −11.2	23:30, 23:22	15, 16	26	4.1×10^4
ducted	*145	−0.48	−49.5, −49.6	−11.8, −11.7	24:04, 24:01	16, 16	37	3.9×10^4
61.40	*594	−6.8	−51.7, −52.5	−9.21, −8.09	18:04, 16:09	16, 16	9	3.9×10^4
	*397	−4.2	−50.2, −51.0	−10.3, −9.29	20:25, 18:54	16, 16	10	3.9×10^4
148.3	dw*1418	−15.	−56.8, −59.1	−5.12, −2.74	12:52, 8:54	16, 16	9	3.7×10^4
ducted	921	−18.	−52.5, −53.6	−5.96, −5.65	9:13, 6:13	16, 10	6	6.0×10^4

Table 4. Forward ray trace results for medium-scale gravity waves.

λ_H (km)	z_{diss}, $z_{\max}$	$z_{\overline{u'w'}/2}$	lon z_{diss}	lat z_{diss}	$\lvert\lambda_z\rvert$ at z_{diss}	flight range	flight time	z_{diss} time	$u'_H w'_{z_{\text{diss}}}/u'_H w'_{16}$
145.1	138	152	−46.15	−14.59	22	935	3.5	28:16	2.0E+07
	145	154	−47.67	−15.09	28	666	2.8	27:46	5.3E+07
71.40	133	148	−47.78	−14.75	17	548	2.8	24:15	1.4E+07
	166	177	−48.73	−14.34	39	370	2.2	24:00	1.1E+08
158.6	120	129	−45.79	−14.94	12	1319	7.8	27:41	4.0E+06
	171	171	−46.33	−14.58	29	1006	5.1	26:43	8.1E+07
64.00	145	162	−47.82	−14.42	25	427	2.0	25:27	3.6E+07
	145	152	−48.27	−14.44	27	329	1.2	25:15	6.2E+07
61.40	110	116	−47.82	−14.45	6	803	8.9	25:59	1.6E+06
	94	94	−48.89	−13.03	20	408	4.3	23:57	1.5E+05
148.3	106	111	−46.53	−15.86	5	1839	19.	30:04	6.8E+05
	113	116	−48.34	−17.18	10	1367	24.	31:49	1.7E+06

kinematic viscosity and thermal diffusivity increase nearly exponentially with altitude, eventually every GW dissipates, although at differing altitudes depending on its characteristics (Vadas and Fritts, 2006; Vadas, 2007). As a GW begins to dissipate, its momentum flux decreases less rapidly with altitude. The altitude where a GW's momentum flux is maximum is called its dissipation altitude, or z_{diss}. Above z_{diss}, the momentum flux decreases rapidly over a scale height or two (Vadas, 2007). We define $z_{\overline{u'w'}/2}$ to be the altitude above z_{diss} where the momentum flux is a factor of 2 smaller than its value at z_{diss}. $z_{\overline{u'w'}/2}$ is a reasonable maximum altitude where this GW can effect significant change on the ionosphere by potentially seeding plasma instabilities prior to dissipating.

On the other hand, a GW can instead dissipate at a critical level if $\omega_{Ir}=0$ or $c_H=U_H$. Additionally, a GW reflects downwards above the OH layer if it becomes evanescent, which occurs if its intrinsic frequency is too large, $\omega_{Ir}>N$, or $m^2<0$. This can occur, for example, if a very high-frequency GW propagates to a region in the thermosphere where the buoyancy frequency is smaller than in the lower atmosphere, or if a high-frequency GW propagates to a region in the thermosphere where it encounters a very large wind moving opposite to the GW's propagation direction.

We now ray trace each medium-scale GW from Table 2 forward in time from its initial location in the OH layer. We employ the same numerical box used previously. Table 4 shows the results. For each GW, rows 1 and 2 show the results when the horizontal winds are zero and equal the model winds, respectively. The columns, from left to right, show the horizontal wavelength λ_H (in km), z_{diss} or $z_{\max}$ (in km),

$z_{\overline{u'w'}/2}$ or $z_{\max}$ (in km), the longitude of $z_{\rm diss}$ or $z_{\max}$ (in deg), the latitude of $z_{\rm diss}$ or $z_{\max}$ (in deg), the value of $|\lambda_z|$ at $z_{\rm diss}$ or $z_{\max}$ (in km), the flight range (i.e. the horizontal distance) from the source to $z_{\rm diss}$ or $z_{\max}$ (in km), the flight time taken to reach $z_{\rm diss}$ or $z_{\max}$ from the source (in hrs), the time that the GW reaches $z_{\rm diss}$ or $z_{\max}$ (in UT), and the ratio of the GW's momentum flux at $z_{\rm diss}$ or $z_{\max}$ to its average momentum flux at the tropopause. Here, $z_{\max}$ is the maximum altitude that a GW attains if, instead of dissipating, it reaches a critical level, it becomes evanescent and reflects downward, or its group velocity exceeds 90% of the sound speed c_s.

The GW with $\lambda_H = 158.6$ km dissipates at $z_{\rm diss}$=120 and 170 km in zero and the model winds, respectively. Thus, this GW penetrates to the highest altitude when the horizontal winds equal the model winds. We will see in the next section that this occurs because the winds are northwestward in the lower thermosphere, therefore enhancing the altitudes attained by southeastward-propagating GWs. Note that $z_{\rm diss}$=$z_{\overline{u'w'}/2}$=171 km for this GW in the model winds because the wave is removed when its group velocity equals $0.9c_s$. It is possible that this wave would continue propagating to higher altitudes, however. For the GWs with λ_H=145.1, 71.4, 158.6, and 64 km propagating through the model winds, the GWs propagate well into the thermosphere prior to dissipating. For the GWs with λ_H=61.4 and 148.3 km, however, the GWs dissipate or encounter critical levels at or below the turbopause. This is because these latter GWs have slow horizontal phase speeds of $c_H \simeq 27-30\,{\rm m\,s^{-1}}$ (see Table 1).

The flight ranges and times from the source to $z_{\rm diss}$ depend on the GW, and vary from 300–1900 km and 1.2–19 h, respectively. For the GWs which penetrate above $z>150$ km, the GWs with λ_H=71.4 and 158.6 km achieve the highest altitudes of $z_{\overline{u'w'}/2} \simeq 177$ and >171 km, respectively. Therefore, these GWs may propagate to high enough altitudes to seed ESF via field-line-integrated modulation of plasma if they are far enough away from the magnetic equator where magnetic field lines are lower in altitude (Fritts et al., 2008). Note that the GW with λ_H=71.4 km has a very short range from the source to $z_{\rm diss}$ of 370 km in the model wind, and therefore is fairly steeply propagating. However, this attribute by itself is not enough to ensure propagation to the bottomside of the F layer. Instead, GWs with larger horizontal wavelengths of 100–400 km propagate most readily to the bottomside of the F layer (Vadas, 2007; Fritts and Vadas, 2008). On the other hand, having a large horizontal wavelength does not, by itself, ensure deep penetration into the thermosphere either. Comparing $z_{\rm diss}$ for the GWs with λ_H=145.1, 158.6, and 148.3 km, we see that relatively deep penetration into the thermosphere is achieved by those GWs with horizontal phase speeds of $c_H > 40\,{\rm m\,s^{-1}}$. Indeed, penetration into the F-region is possible for GWs having medium-scale horizontal wavelengths of $\lambda_H \sim 100-200$ km, but with intrinsic horizontal phase speeds of $c_{IH} > 100\,{\rm m\,s^{-1}}$ (Vadas, 2007).

5 Convective sources and penetration into the thermosphere

In this section, we show details of the reverse and forward ray tracing of the medium-scale GWs described in the previous section. We then superimpose these results on satellite images as near as possible to the source times. Because deep convection tends to occur for several hours within a localized region of a few square degrees, and because the horizontal sizes and updraft velocities of the convective plumes and clusters in this region are reasonably constant, identification of the convective plume or region which likely excited a GW can be used to model the spectrum of GWs excited from a typical convective plume in this region, in order to ray trace this spectrum into the thermosphere to determine its amplitudes and scales there.

In Figs. 7 and 8, the ray paths of the medium-scale GWs as a function of time and altitude are shown in the left column, and the ray-paths as a function of longitude and latitude are shown in the middle column. Figure 7 shows the GWs with λ_H=145.1, 71.4, and 158.6 km during late September and early October, while Fig. 8 shows the GWs with λ_H=64.0, 61.4, and 148.3 km during late October. Results with zero winds and the model winds are shown as dash and solid lines, respectively. Note that the x and y scales of the plots in the left and middle columns vary in order to show the details of the ray tracing. In order to better understand the role that winds play in GW penetration in the thermosphere, the right column shows the zonal (solid) and meridional (dash) model winds at the location of the all-sky imager at the GW's start time. Positive zonal (meridional) winds are eastward (northward). Note that the winds vary with latitude, longitude, altitude, and time, as discussed previously.

5.1 GW on 30 September–1 October with λ_H=145.1 km

On the night of 30 September 2005, only one medium-scale GW was observed by the all-sky imager: the GW with λ_H=145.1 km. This GW was reasonably fast, had a fairly localized source 400–500 km away, and propagated reasonably far into the lower thermosphere prior to dissipating. Although this eastward propagating GW had a large enough horizontal wavelength to reach the bottomside of the F layer in theory, the background winds were not favorable, since the zonal winds were $\sim$0 at $z \sim 150$ km. Thus, although this GW avoids critical levels and evanescence above the OH layer, it dissipates at $z \sim 145-155$ km. If the winds are zero, this GW travels straight in the longitude/latitude plot (dash line in Fig. 7b). When the winds equal the model winds, the path taken is quite contorted. Above the OH layer, the GW propagates rapidly southward because of the strong southward meridional wind at $z \sim 90-100$ km (dash line in Fig. 7c). However, the GW then propagates rapidly northward because of the strong northward meridional winds at $z \sim 110-120$ km. Thus, this GW is buffetted around by the

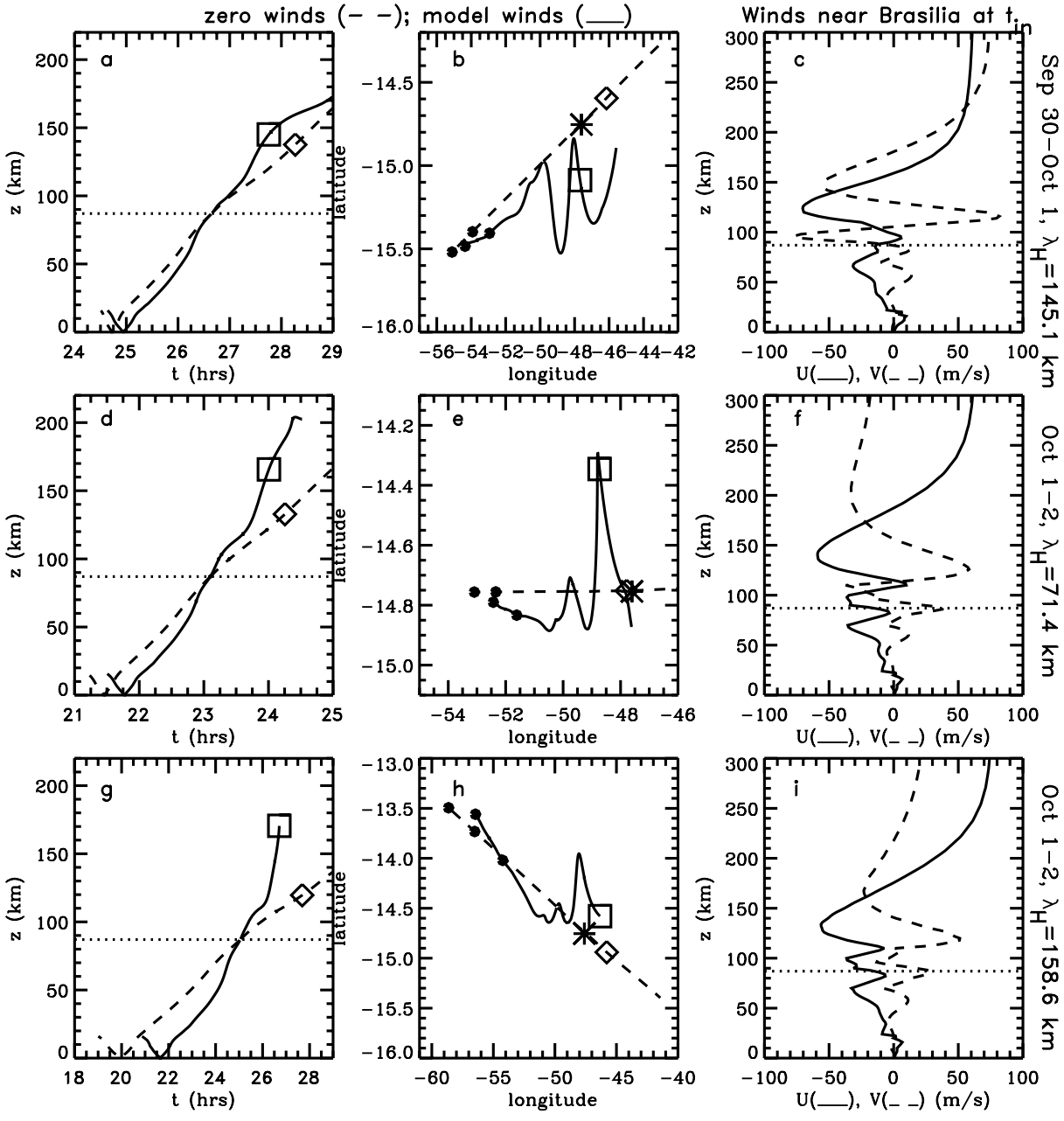

Fig. 7. Reverse and forward ray trace results for the medium-scale GWs observed in late September and early October. Row 1: GW with λ_H=145.1 km. Row 2: GW with λ_H=71.4 km. Row 3: GW with λ_H=158.6 km. Column 1: Altitude as a function of time. Dash and solid lines show the ray paths for zero winds and the model winds, respectively. The dotted line shows OH airglow altitude. Column 2: Flight path in latitude and longitude. Solid and dash lines are the same as in column 1. Black dots show the locations of sources "1" and "2". Diamonds and squares denote $z_{\rm diss}$ for zero winds and the model winds, respectively. The asterisk denotes the location of the all-sky imager. Column 3: Zonal (solid) and meridional (dash) model winds at the location of the all-sky imager at the start time for each GW.

large meridional winds in the lower thermosphere. From Fig. 7b, the convective source region is southwest of the all-sky imager.

According to Table 3, this GW was excited at the tropopause on 1 October from sources "1" and "2" at 00:40 and 01:20 UT, respectively, using the model winds, and from sources "1" and "2" at 00:30 and 01:00, respectively, using zero winds. Figure 9 shows infrared satellite images on 30 September at ∼23:50 UT, which is approximately 40–80 min prior to these source times. The upper panel shows a satellite image which has been color coded for temperatures from $-66^{\rm o}$C to $-76^{\rm o}$C, and the lower panel shows the brightness

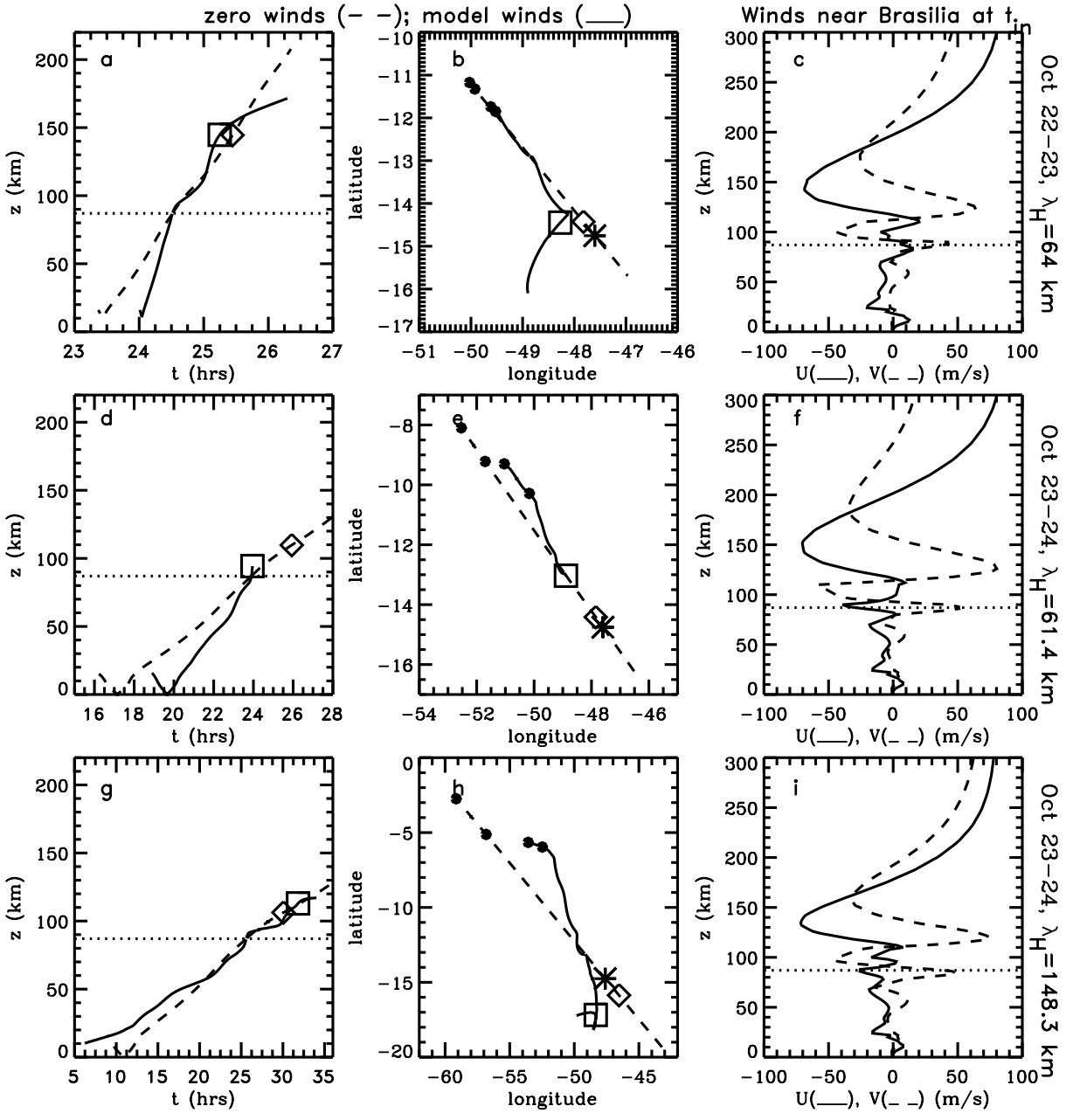

Fig. 8. Same as in Fig. 7, but for the medium-scale GWs observed in late October. Row 1: GW with λ_H=64 km. Row 2: GW with λ_H=61.4 km. Row 3: GW with λ_H=148.3 km.

temperature. Note that localized cold temperatures on the anvils imply areas where cloud material is higher (via convective overshoot) than surrounding anvil material (Heymsfield and Blackmer, 1988). The peach-colored, 4-pointed stars show the location of the all-sky imager near Brasilia. The purple stars show the approximate locations of sources "1" and "2" using the model winds, and the blue stars show the approximate locations of sources "1" and "2" for zero winds. The green stars show the approximate GW dissipation locations for the model and zero winds. Small, localized clouds are seen ∼100 km south and southeast of the eastern purple star. The lower panel of Fig. 9 shows the brightness temperature. We see one localized cold region at -16.5^o latitude and -52^o longitude, and a smaller region at -17.5^o latitude and -52.5^o longitude, which suggest deep convective plumes and convective overshoot. Both plumes are within 100 km of source "2" through the model winds (eastern purple star). We can verify that the updraft velocity of a plume in this region would have been energetic-enough to excite GWs by examining the Convective Available Potential Energy (or

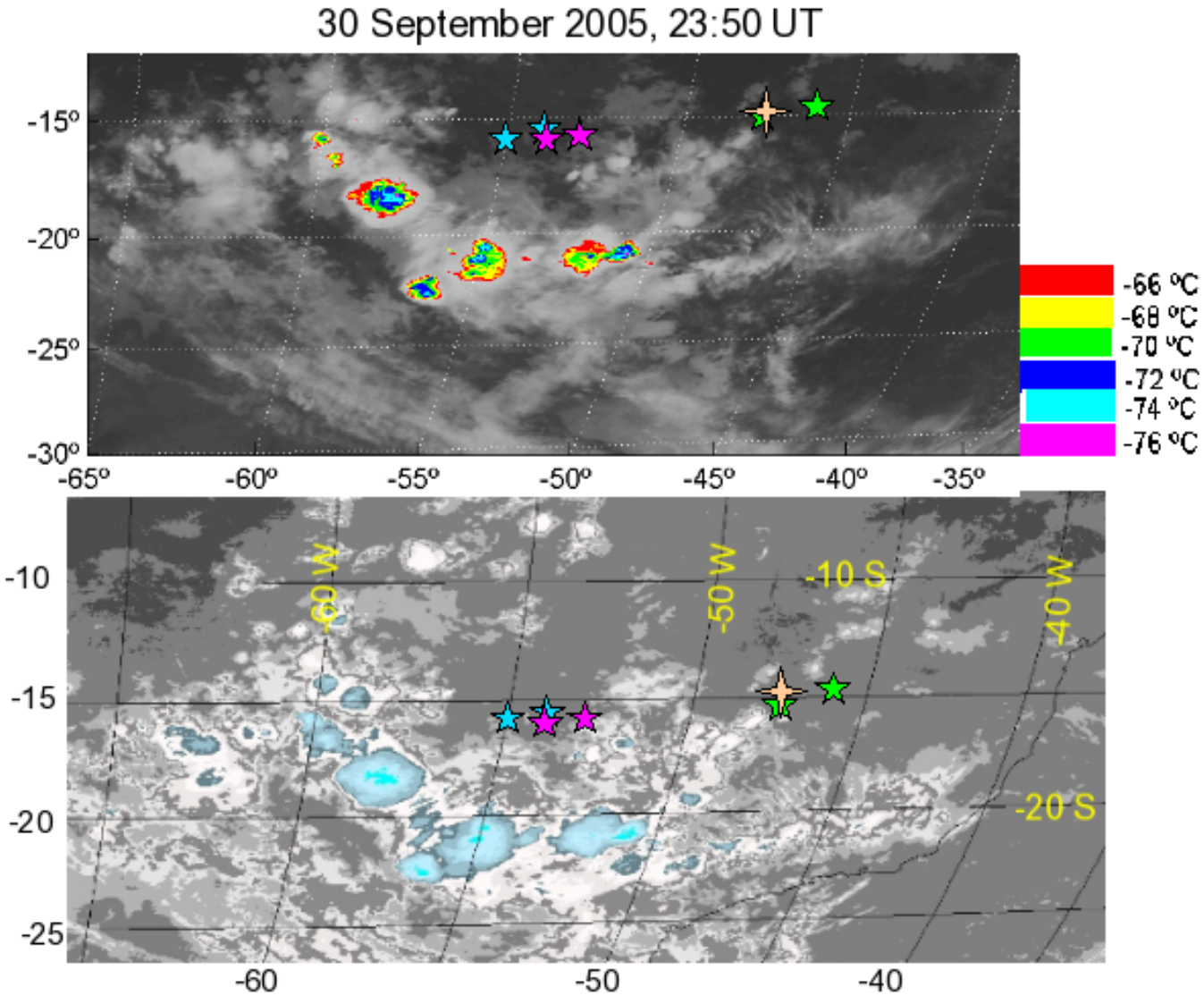

Fig. 9. Infrared satellite images on 30 September at ∼23:50 UT. The locations of sources "1" and "2" for the GW with λ_H=145.1 km through the model winds (zero winds) are shown as purple (blue) stars. The locations of $z_{\rm diss}$ are shown as green stars. The location of the all-sky imager is shown as a 4-pointed peach star.

CAPE) (Bluestein, 1993). Figure 10 shows a CAPE map on 1 October at 00:00 UT. At this time, the CAPE is substantial at this source location, with a value of 800–1000 J/kg. The CAPE is the maximum kinetic energy per mass available to a parcel of air. Therefore, the maximum upward velocity for a convective plume in this region is

$$w \sim \sqrt{2\,\mathrm{CAPE}}. \tag{13}$$

Although Eq. (13) may be interpreted as an upper limit for the maximum updraft velocity of a convective plume in this area, a balloon experiment showed that the velocity of the updraft equaled Eq. (13) for one storm (Bluestein et al., 1988). Therefore, we set the plume velocity to roughly equal Eq. (13). For this area then, the updraft velocity was w∼40−44 m/s, consistent with an energetic convective plume with sufficient overshoot into the stratosphere to excite GWs. Therefore, we estimate that the convective plume which created this medium-scale GW was likely located at a longitude of −52° and a latitude of −16.5° at ∼01:00 UT on 1 October. We also note from Fig. 9 that there is a large convective cluster at 58° W and 18° S, which is ∼400−700 km beyond the estimated source location in the same propagation direction. However, because the GW's amplitude agrees very well with the model amplitude for a small convective plume (see Sect. 6.2), and because this source is much farther from the model source locations than the plume at 52° W and 16.5° S, this convective cluster is not the likely source of this GW.

In conclusion, the closest modeled location occurs for source "2" with the model winds, which is within 100 km of a deep convective plume located at 52° W and 16.5° S at ∼01:00 UT on 1 October. This implies that the excited GW was initially upward-propagating, and propagated directly through the model winds to the OH airglow layer. We denote this "best fit" with $^{up}*$ in Table 3 for this GW, where "up" stands for upward-propagating. Note that this GW's dissipation location is nearly directly above the all-sky imager for the model winds.

5.2 GW on 1–2 October with λ_H=71.4 km

On the night of 1 October 2005, two medium-scale GWs were observed by the all-sky imager, the GWs with λ_H=71.4 km and λ_H=158.6 km. From Table 3, their source times are similar: ∼21:00–22:00 UT and ∼19:00–22:20 UT, respectively. We first focus of the GW with λ_H=71.4 km. This GW dissipates at the highest altitude when the winds equal the model winds, i.e. $z_{\rm diss}$∼170 km (see Table 4). If the winds are zero, this GW instead dissipates at $z_{\rm diss}$∼135 km. Figure 7f explains why this occurs. There is a strong northwestward wind at z∼120−150 km, which causes the vertical wavelength for this southeastward propagating GW to increase, since the GW is propagating opposite to the winds. Larger λ_z allows for deeper penetration into the thermosphere (Vadas, 2007).

According to Table 3, this GW was excited at the tropopause on 1 October from sources "1" and "2"at 21:30 and 22:00 UT, respectively for the model winds, and from sources "1" and "2" at 21:10 and 21:40, respectively for zero winds. Figure 11 shows infrared satellite images on 1 October at 21:22 UT (upper panel) and 21:52 UT (lower panel). The estimated locations of sources "1" and "2" are shown as purple (blue) stars when the winds equal the model winds (zero winds). We see that there is a single, energetic, convective plume 500 km due west of Brasilia at a longitude of −52.5° and a latitude of −15°. This plume was strong at 21:22 UT, but faded somewhat by 21:52 UT. Note that when the winds equal the model winds, source "1" is only ∼1/4−1/2° east of this convective plume; even better agreement is obtained for source "1" for zero winds. Figure 12 shows a CAPE map on 1 October at 18:00 UT, 3 h before Fig. 11. At this time, the CAPE is 600−800 J/kg at the location of the convective plume, which yields an upward plume velocity of w∼35−40 m/s from Eq. (13). This is sufficient to excite GWs via convective overshoot.

In conclusion, the localized but energetic convective plume which created this medium-scale GW was centered at a longitude of −52.5° and a latitude of −15°. The closest modeled location occurs for source "1" with zero winds, which is within 0–10 km of this deep, convective plume (see western blue star). This implies that the excited GW was initially downward-propagating, reflected off the Earth's surface, then propagated through zero winds to the OH airglow layer. We denote this "best fit" with $^{dw}*$ in Table 3 for this GW, where "dw" stands for downward-propagating. Note that this fit is the best of the six GWs.

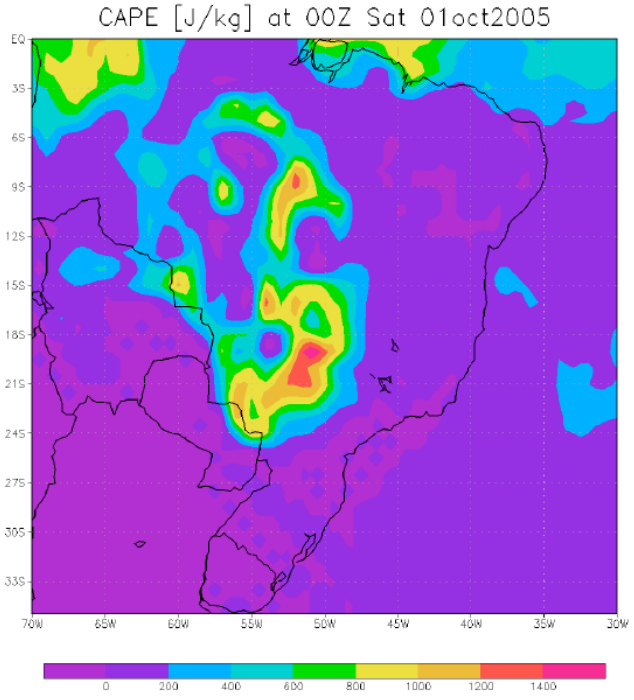

Fig. 10. A map of the CAPE on 1 October at 00:00 UT.

5.3 GW on 1–2 October with λ_H=158.6 km

We now focus on the GW with λ_H=158.6 km. In theory, this GW could penetrate to high altitudes in the thermosphere if the winds are large and oppositely-directed, because its horizontal wavelength is large enough. From Table 4, this GW has a significant wave amplitude to $z_{\rm diss}$=$z_{\overline{u'w'}/2}$∼171 km, where ray tracing ends because the group velocity equals $0.9c_s$. From Fig. 7i, the model winds are northwestward at z∼120−150 km, which causes λ_z to increase, thereby accelerating its vertical propagation velocity and increasing the dissipation altitude as compared to zero winds. However, the winds are southwestward at z≃150 km, thereby decreasing λ_z somewhat. It may be possible to seed ESF and plasma bubbles via field-line-integrated modulation of plasma at an altitude as low as z≃170 km (Fritts et al., 2008), but at magnetic latitudes of ∼±10° (Abdu, personal communication). From Fig. 7h, the convective source region estimated from ray tracing is northwest of the all-sky imager at at 13−14° S, very close to the magnetic equator.

According to Table 3, this GW was excited at the tropopause on 1 October from sources "1" and "2"at 20:50 and 22:20 UT, respectively using the model winds. Figure 13 shows an infrared satellite image on 1 October at 20:53 UT (upper panel) and 22:22 UT (lower panel), corresponding to

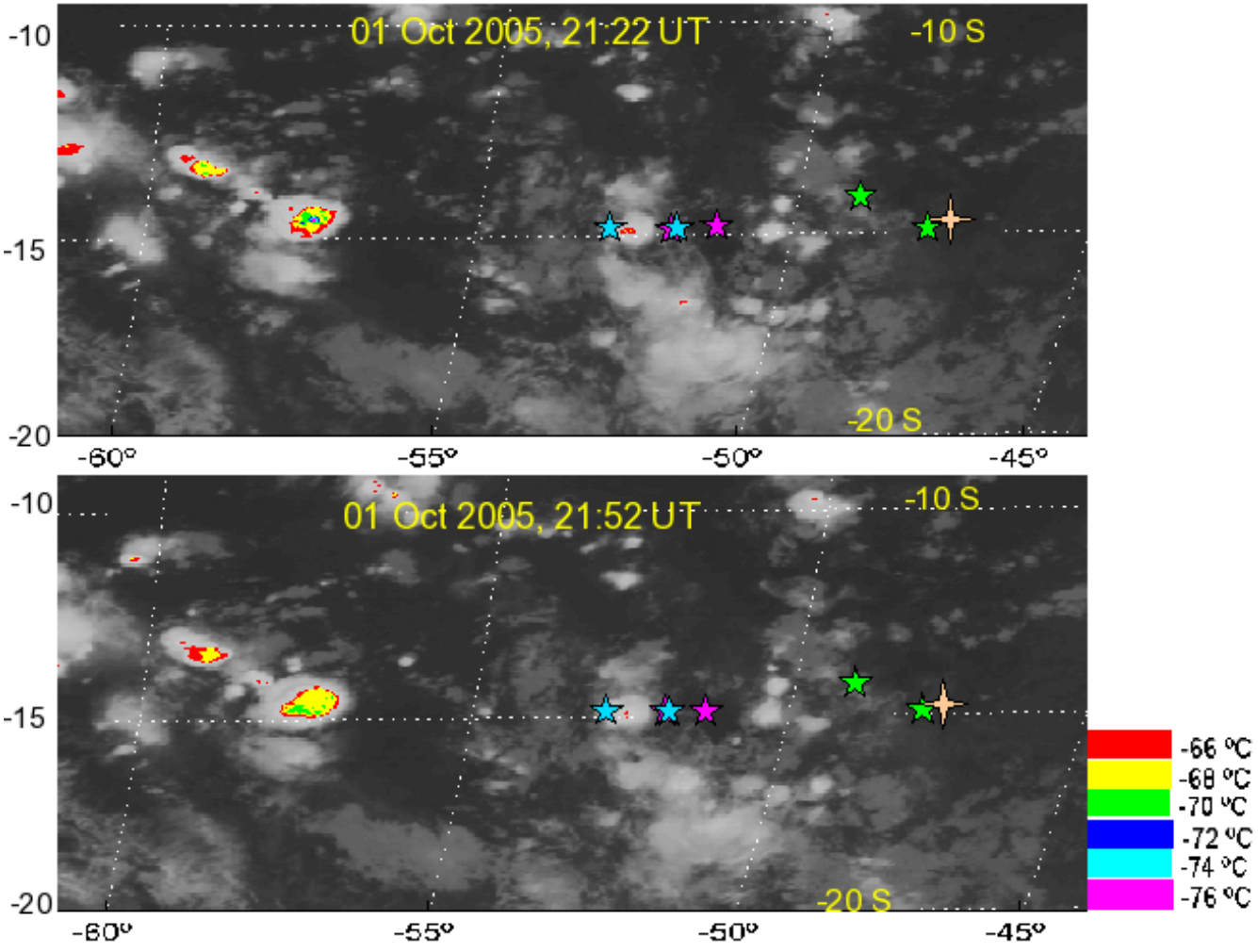

Fig. 11. Infrared satellite images on 1 October at 21:22 UT (upper panel) and at 21:52 UT (lower panel). The locations of the sources and $z_{\rm diss}$ for the GW with λ_H=71.4 km are shown using the same symbols as in Fig. 9.

sources "1" and "2", respectively. The estimated locations of sources "1" and "2" are shown as purple stars in the upper and lower panels, respectively. There is a large, strong convective cluster at 58° W and 14.5° S corresponding to source "1" at 20:53 UT. This source is ∼150−200 km southwest of the purple star. Instead, if the winds are zero, then the times of sources "1" and "2" are 19:00 and 20:40 UT from Table 3. Figure 14 shows a satellite image at 18:52 UT. The location of source "1" for zero winds is shown with the blue star in Fig. 14, and the location of source "2" for zero winds is shown with the blue star in the upper panel of Fig. 13. We see that the source locations are again within 1−2° of several active convective regions at both times. In particular, there is a large convective cluster at 58° W and 14.5° S corresponding to source "1" or "2" at 20:53 UT. At 18:52 UT, there are several small convective plumes at (58° W, 13° S), (59° W, 12.5° S), and (59° W, 14° S). There is also an energetic small convective cluster at (58° W, 15° S); these correspond to source "1" through zero winds. All of these plumes are within the same convective region: 57−60° W and 12−15° S.

In conclusion, although it is difficult to determine the exact convective plume or cluster which excited this medium-scale GW, it is very likely that this GW was excited from a convective plume or a small/large convective cluster located at 57−60° W and 12−15° S from 19:00–21:00 UT. The modeled sources occur within 20–100 km of a deep, convective plume. We denote these "best fits" with asterisks in Table 3 for this GW.

5.4 GW on 22–23 October with λ_H=64.0 km

We now investigate the medium-scale GW which was observed on 22–23 October with λ_H=64 km. From Table 4, this GW dissipated at $z_{\rm diss}$∼145 km. This GW does not propagate to the bottomside of the F layer because λ_H is not large enough to overcome dissipation in the E-region. From

Fig. 8b, the convective source region estimated from ray tracing is northwest of the all-sky imager.

According to Table 3, this GW was excited at the tropopause at 23:20–24:00 UT. The zero and model wind results are similar (see Fig. 8b). The locations and times of sources "1" and "2" are also similar, because the GW reflects upwards at $z\sim$10 km. On this day we only have satellite images every 3 h. Figure 15 shows infrared satellite images on 22 October at 23:54 UT, very close to the estimated source times. The estimated sources and dissipation locations are displayed. We see that there is no convective activity near the estimated sources. There is, however, a longitudinal band of deep convection along the same propagation direction 500–700 km to the NE of the modeled source location; this region is easily seen on the brightness temperature image (lower panel). It is possible that this GW was excited from one of the deep, convective plumes at $-6-7^o$ latitude and $-52-54^o$ longitude. Because these convective plumes are oriented along the direction from the all-sky imager to the modeled source locations, we conclude that this GW was probably excited from one of these convective plumes, then was ducted approximately 500–700 km before reaching the OH layer over the all-sky imager near Brasilia. This distance is within reasonable limits given by modeling studies of wave ducting (Walterscheid et al., 1999; Hecht et al., 2001). In conclusion, the deep convective plume which probably excited this medium-scale GW was located at a longitude of $-52-54^o$ and a latitude of $-6-7^o$ at ~24:00 UT. The modeled source is ~500–700 km short (along the same propagation direction), thereby suggesting that the GW was ducted. It is also possible that the winds in the OH layer were very different from that estimated here, that this GW is a large-amplitude secondary GW from wave breaking, or that this GW was excited from a different source.

5.5 GW on 23–24 October with λ_H=61.4 km

On the night of 23–24 October 2005, two medium-scale GWs were observed. We examine the GW with λ_H=61.4 km first. This GW propagated slowly upwards from the troposphere to the OH airglow layer in 4–7 h. From Table 4, this GW dissipates by $z\sim$110 km. If the winds equal the model winds, then this wave is removed at $z\sim$94 km because it attained a group velocity greater than $0.9c_s$. Thus, this GW is not expected to play a significant role in the thermosphere.

According to Table 3, this GW was excited at the tropopause from sources "1" and "2" at 19:00 and 20:30 UT, respectively, for the model winds, and at 16:00 UT and 18:00 UT, respectively, if the winds are zero. Thus the source time for this GW is fairly uncertain. As before, we only have satellite images every 3 h on this day. Figure 16 shows the satellite image on 23 October at 17:54 UT (upper panel) and at 20:54 UT (lower panel). The estimated sources and dissipation locations are also displayed. We see that there is a deep, convective plume and a small convective cluster

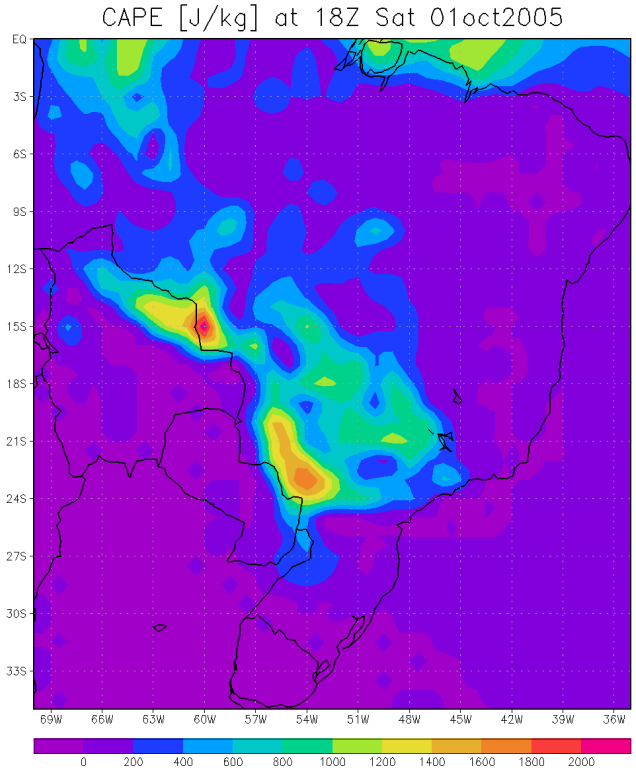

Fig. 12. A map of the CAPE on 1 October at 18:00 UT.

within 50 km of the ray traced source "2" at 20:54 UT for the model winds. Additionally, there is also active convection within 100 km of the ray traced source "1" through the model winds at 17:54 UT. For zero winds, there are deep convective plumes and small convective clusters within 100 km of sources "1" and "2" at 17:54 UT. Because of source time and location uncertainties, and because of the large number of deep convective plumes and clusters, we cannot determine the exact source of this wave; we can only determine the convective region which likely excited this GW.

In conclusion, because of uncertainties, both the zero and model winds comprise good fits to the excitation of this GW from a deep convective plume or cluster at $50-53^o$ W and $8-10^o$ S at 16:00–21:00 UT. Additionally, the GW could have been either initially upward or downward-propagating. The closest modeled location is 50–100 km from the nearest deep convective plume, although we do not know which convective plume or cluster this GW was excited from. We denote these "best fits" with asterisks in Table 3 for this GW.

5.6 GW on 23–24 October with λ_H=148.3 km

The second GW observed on 23–24 October was the medium-scale GW with λ_H=148.3 km. This GW propagated slowly upwards from convective sources northwest of the all-sky imager, in ~15–18 h, and does not does not penetrate far above the turbopause.

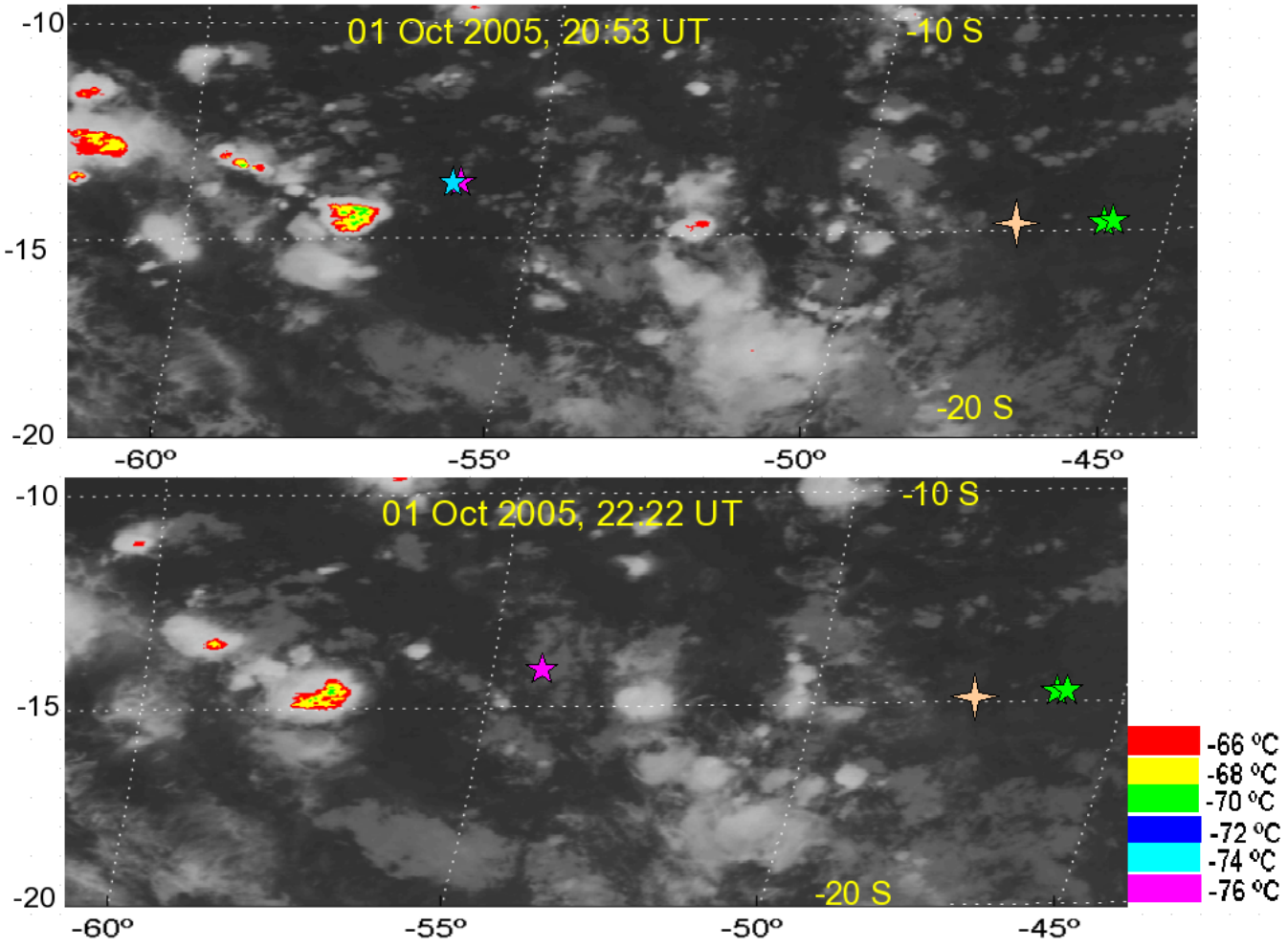

Fig. 13. Infrared satellite images on 1 October at 20:53 UT (upper panel) and at 22:22 UT (lower panel). The locations of the sources and $z_{\rm diss}$ for the GW with λ_H=158.6 km for the model winds (both panels) and zero winds (source "2", upper panel only) are shown using the same symbols as in Fig. 9.

According to Table 3 and Fig. 8g, this GW was excited at the tropopause at ∼09:00 UT from source "2" for the model wind case. The estimated times for sources "1" and "2" for zero winds are quite different: ∼09:00 and 13:00 UT, respectively. Therefore, the error in the source times is several hours. As before, we only have satellite images every 3 h on this day. Figure 17 shows the satellite image on 23 October at 08:54 UT (upper panel), and at 11:45 UT (lower panel). We see the edge of a strong convective cell (or small cluster) at 0° latitude and −62.5° longitude at 08:45 UT, and a few small convective clusters at −1° latitude and −62−63° longitude at 11:45 UT, along the same direction as the modeled source locations. No other convective regions along this direction are observed. Note that source "1" is closer to the convective source when the winds are zero, although it is still ∼700 km short of this convective region. This implies that this GW was probably ducted ∼700 km to the OH layer above the all-sky imager. Thus, this GW was probably a downward-propagating GW excited from a small convective cluster at −1° latitude and −62.5° longitude at 09:00 UT. Note that this GW reflects upwards from the Earth's surface 300 km from the source in this scenario.

In conclusion, the closest modeled location occurs for source "1" with zero model winds (blue star). This implies that the GW was probably excited from a small convective cluster at 62.5° W and 1° S, propagated downwards initially, reflected off the Earth's surface, and propagated through zero winds to the OH airglow layer. It also suggests that the GW was probably ducted ∼700 km, although it is possible that very different (and oppositely-directed) winds can account for this difference. Additionally, other excitation mechanisms are possible. We denote this "best fit" with ${}^{dw}*$ in Table 3 for this GW.

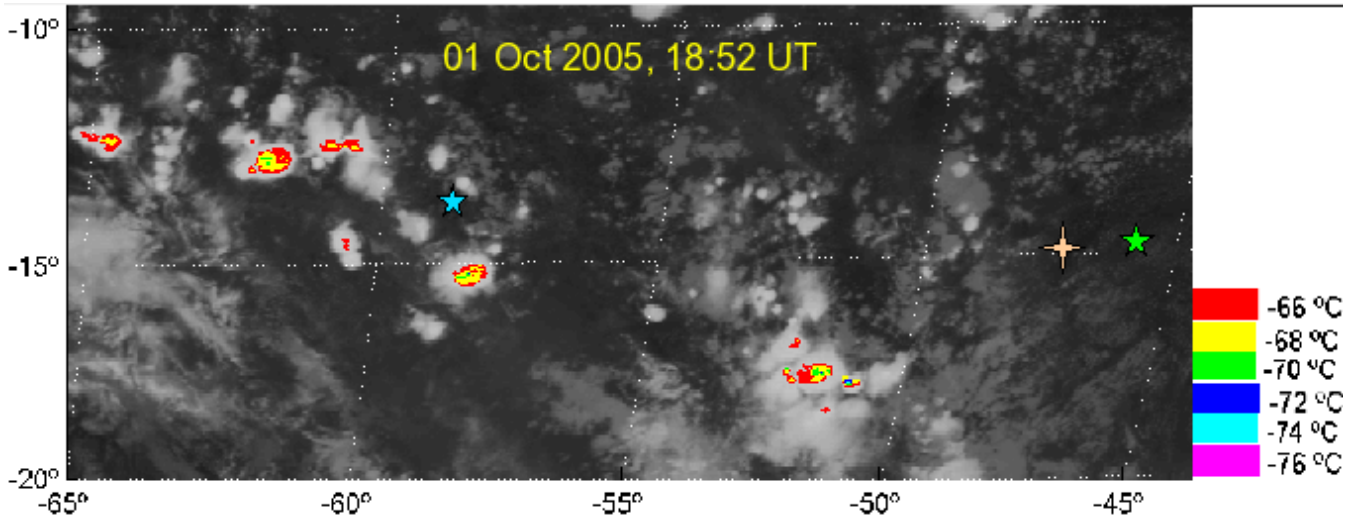

Fig. 14. Infrared satellite images on 1 October at 18:52 UT. The location of source "1" and $z_{\rm diss}$ for the GW with λ_H=158.6 km for zero winds are shown using the same symbols as in Fig. 9.

6 Wave amplitudes and convective plumes

6.1 Gravity wave amplitudes

We now estimate the GW amplitudes in the OH airglow layer. Our goal is to use these estimates to constrain the convective plume parameters that determine these momentum fluxes, and to estimate the wave amplitudes and momentum fluxes of the other GWs in the excited convective spectrum that more easily reach the bottomside of the F layer (Fritts et al., 2008).

Each GW's amplitude is inferred from its fractional intensity perturbations, $\mathrm{I}'/\overline{I}$, and the cancellation factor, CF (Liu and Swenson, 2003):

$$\mathrm{CF} = (\mathrm{I}'/\overline{I})/(\mathrm{T}'/\overline{T}). \tag{14}$$

For these medium-scale GWs, CF ranges from 1.9 to 3.6, and depends on λ_z. The dependence on λ_z arises because the intensity perturbations in the OH airglow layer partially cancel out for λ_z<20−30 km due to the finite thickness of the OH layer. GW horizontal wind perturbations can be written as (Fritts and Alexander, 2003)

$$u'_H \sim (mg\omega_{Ir}/k_H N^2)\theta'/\overline{\theta}, \tag{15}$$

assuming adiabatic motions. For hydrostatic GWs satisfying $\omega_{Ir}^2 \ll N^2$, $m/k_H \sim N/\omega_{Ir}$, and $\theta'/\overline{\theta}=\mathrm{T}'/\overline{T}$, Eq. (15) becomes

$$u'_H \sim (g/N)\mathrm{T}'/\overline{T}. \tag{16}$$

For $g \simeq 9.5\,\mathrm{m/s^2}$ and $N \sim 0.01\,\mathrm{s^{-1}}$,

$$u'_H \sim 10^3\,\theta'/\overline{\theta}\ \mathrm{m/s}. \tag{17}$$

Thus, a 1% temperature or potential temperature perturbation corresponds to a GW horizontal velocity perturbation of $u'_H \sim$10 m/s. From the Boussinesq continuity equation, we estimate a GW vertical velocity perturbation of

$$w' \sim -k_H u'_H/m \tag{18}$$

and an average momentum flux of

$$\overline{u'_H w'} \sim 0.5(k_H/m)(u'_H)^2, \tag{19}$$

where the overline denotes a spatial or temporal average over the GW phase here. The various GW parameters and resulting momentum flux estimates are shown for the six medium-scale GWs in Table 5. The columns, from left to right, show the horizontal wavelength λ_H (in km), $|\lambda_z|$ in the OH layer from Table 2 for the model winds (in km), CF(using $|\lambda_z|$ from column 2), $I'/\overline{I}$ (in %) from Table 1, $T'/\overline{T}$ calculated from Eq. (14) (in %), u'_H from Eq. (16) (in m/s), w' from Eq. (18) (in m/s), and the average momentum flux $\overline{u'_H w'}$ from Eq. (19) (in $\mathrm{m^2/s^2}$). Note that both the vertical velocities (∼1.8 to 4.3 m/s) and the momentum fluxes (∼10 to 50 $\mathrm{m^2\,s^{-2}}$) are within reasonable ranges of observed quantities, especially when we note that these events are likely among the larger and more coherent events observed during the SpreadFEx.

6.2 Horizontal wind spectra of convective plumes

We now show how these medium-scale GWs fit into modeled GW spectra excited from deep convective plumes. We calculate the excited GW spectrum from a convective plume envelope which is 20 km wide, 10 km deep, lasts for 12 min, and has an updraft velocity of 40 m/s. This spectrum is generated from a simple convective plume model which includes ground reflection, neglects small-scale updrafts, and neglects shear in the troposphere (Vadas and Fritts, 2009). Since there

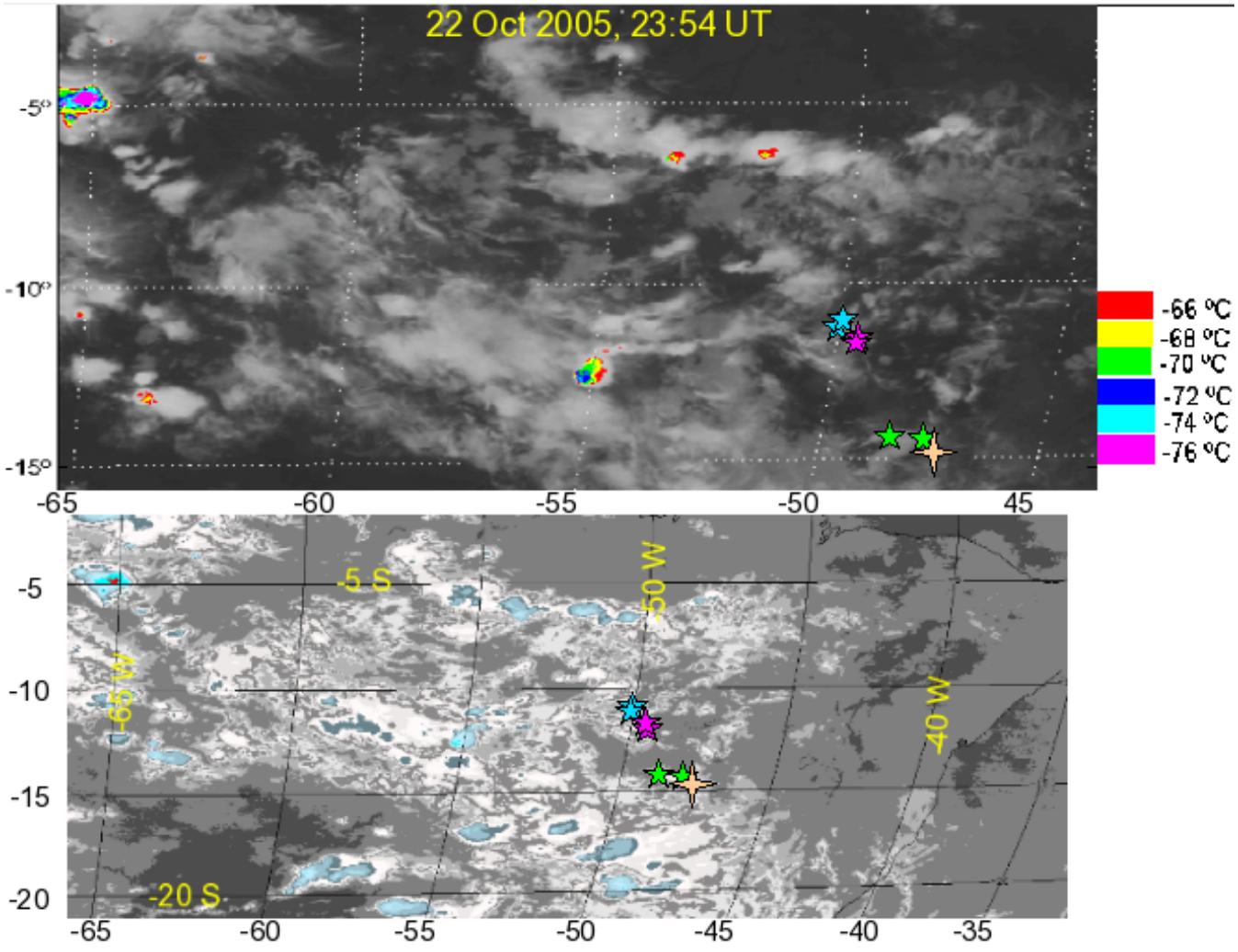

Fig. 15. Infrared satellite images on 22 October at 23:54 UT. The locations of the sources and $z_{\rm diss}$ for the GW with λ_H=64.0 km are shown using the same symbols as in Fig. 9.

Table 5. Calculated GW amplitudes from $I'/\overline{I}$.

λ_H	$\lvert\lambda_z\rvert$	CF	$I'/\overline{I}$	$T'/\overline{T}$	u'_H	w'	$\overline{u'_H w'}$
145.1	27	3.0	3.8	∼1.3	∼12	∼2.2	∼13
71.40	24	2.8	3	∼1.1	∼10.2	∼3.4	∼17
158.6	23	2.6	7	∼2.7	∼25.6	∼3.7	∼48
64.0	44	3.6	2	∼0.6	∼5.3	∼3.6	∼10
61.4	29	3.2	3.1	∼1.0	∼9.2	∼4.3	∼20
148.3	18	1.9	2.9	∼1.5	∼14.5	∼1.8	∼13

are many small-scale updrafts within a convective plume envelope, only a fraction of the air is moving upwards at the tropopause at a given time t. We take this into account by multiplying each excited GW's amplitude by a "filling factor" ϵ. This factor equals 1 if all of the air within the envelope is upward-moving at the tropopause at t, and equals 0.5 if only 1/2 of the volume of air within the convective plume envelope is upward-moving at the tropopause at t. Here, we choose ϵ=0.75, as this gives good agreement with observations of concentric rings in the OH layer (Vadas et al., 2009).

Figure 18a shows the GW horizontal wind amplitudes at z=87 km if the winds are zero, using the spectral form determined by Vadas and Fritts (2009). These amplitudes are the maximum amplitudes that a GW can have at that altitude; they therefore provide an upper bound. Triangles show the horizontal wavelengths of each GW as a function of its average vertical wavelength at the tropopause when the winds equal the wind model (see column 7 from Table 3). We see that these medium-scale GWs have horizontal scales that are consistent with the horizontal scales excited from this convective plume. For this deep convective plume, the model amplitudes corresponding to these medium-scale GWs (at

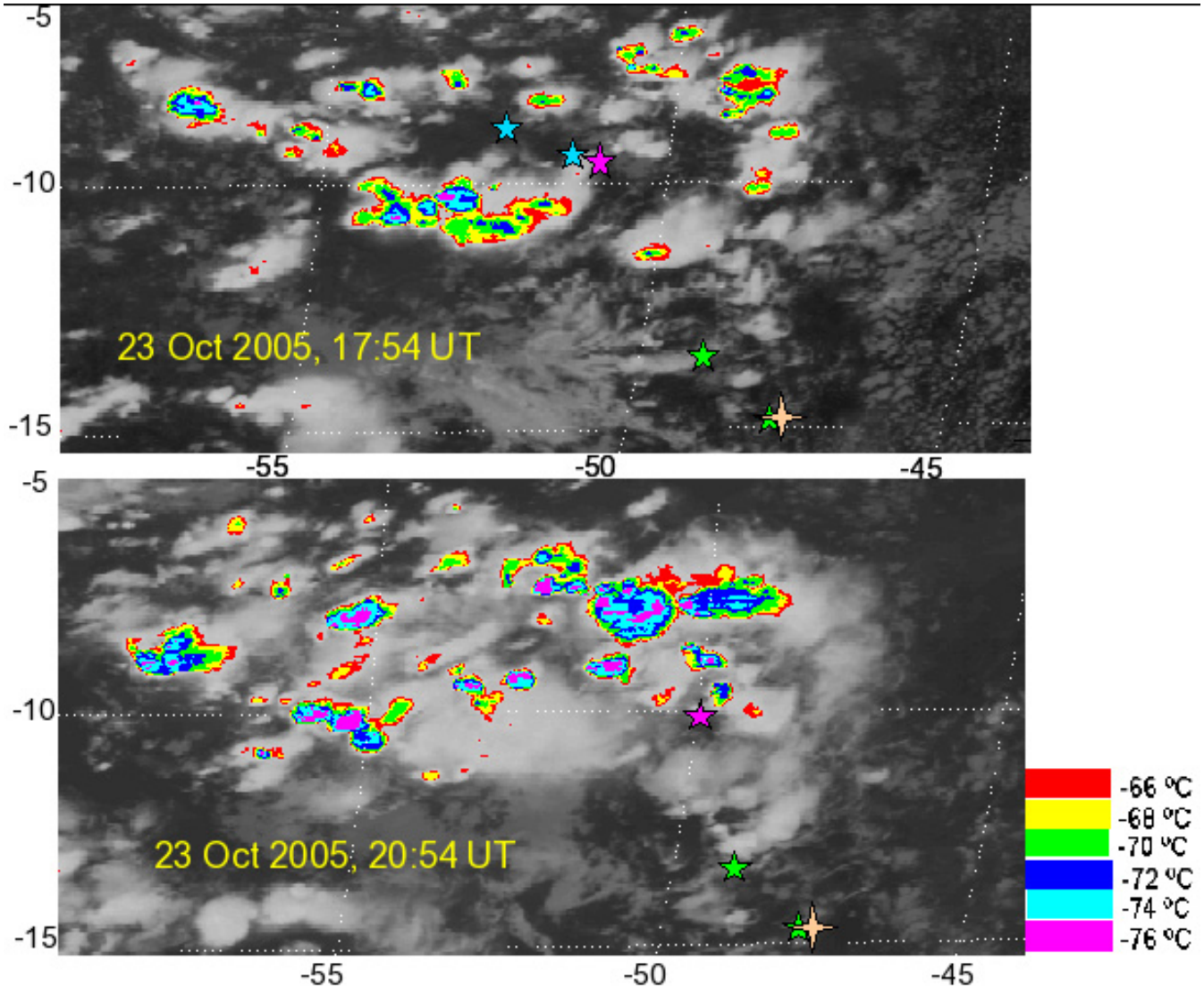

Fig. 16. Infrared satellite images on 23 October at 17:54 UT (upper panel) and at 20:54 UT (lower panel). The locations of the sources and $z_{\rm diss}$ for the GW with λ_H=61.4 km are shown using the same symbols as in Fig. 9.

the location of the triangles) are shown in the first column of Table 6.

We now compare these model amplitudes for a single convective plume with the inferred wave amplitudes, u'_H, using Table 5. We see that the measured and model amplitudes are quite similar for the GWs with λ_H=145.1, 71.4, and 61.4 km. Note that factor of ∼2 discrepancies can be caused by differing updraft velocities or plume diameters. For the GWs with λ_H=158.6 and 148.3 km, however, the observed amplitudes are much larger than the model amplitudes for a single convective plume. This large discrepancy may imply that these GWs were instead excited from a convective cluster. Indeed, as discussed previously, the GW with λ_H=158.6 km may have been excited from the large convective cluster at 58^o W and 14.5^o S at ∼20:50 UT (see Sect. 5.3

Table 6. Maximum model amplitudes.

λ_H	u'_H (single plume)	u'_H (small cluster)
145.1	10−15	30
71.40	15	25−35
158.6	1	1−5
64.0	30−35	60−65
61.4	5	5−15
148.3	<1	<1

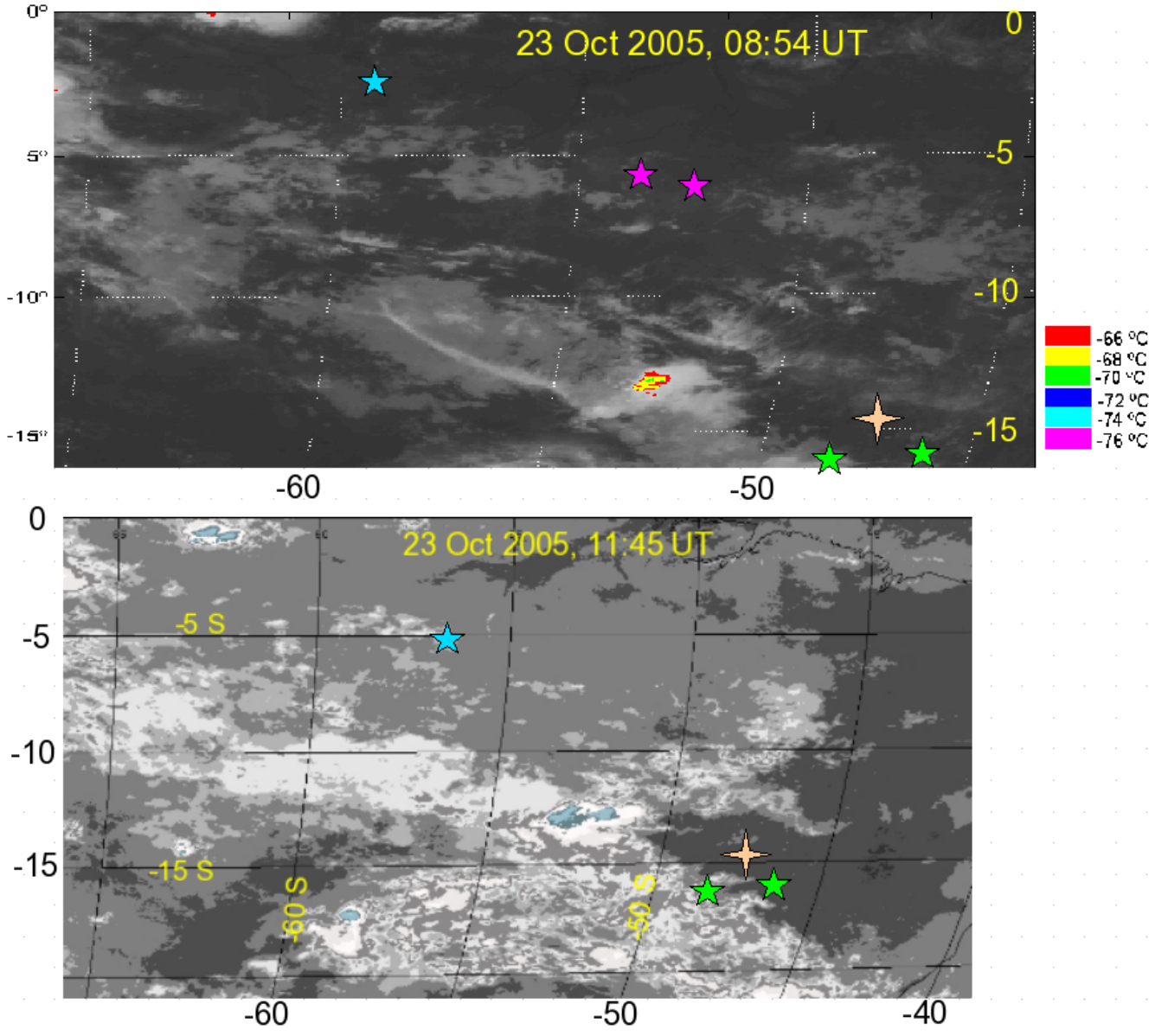

Fig. 17. Infrared satellite image on 23 October at 08:54 UT (upper panel) and at 11:45 UT (lower panel). The locations of the sources and $z_{\rm diss}$ for the GW with λ_H=148.3 km are shown using the same symbols as in Fig. 9.

and the upper panel of Fig. 13). Additionally, the GW with λ_H=148.3 km was likely excited by a small convective cluster (see Sect. 5.6 and Fig. 15). Such large clusters are not described by the GW spectrum shown in Fig. 18a. In fact, it is expected that for large clusters, the amplitudes of GWs with $\lambda_H \sim$100s km and λ_z of order the depth of the troposphere (i.e. $\sim$10−20 km) would be much larger than in Fig. 18a.

For the GW with λ_H=64.0 km, the model amplitude is much larger than the measured amplitude. However, this GW was likely ducted if it was excited from a convective source (see Sect. 5.4); therefore it is not surprising that its measured amplitude is so different from its model amplitude, because different winds result in different values of λ_z at the tropopause, thereby moving the triangle to a different position on the GW spectrum. For example, if λ_z is doubled or halved, then the observed and model values would be in good agreement. Finally, the GWs with λ_H=158.6 and 148.3 km have $\lambda_z \lesssim$10 km. It is possible that the GWs with large λ_H and small $\lambda_z \lesssim$10 km are not well represented by this convective plume model, since it has only been successfully tested on GWs seen in the OH airglow layer with $\lambda_H \sim$20−100 km and $\lambda_z \sim$20−40 km (Vadas et al., 2009).

We also show the GW spectrum excited from a small convective cluster in Fig. 18b. This small convective cluster

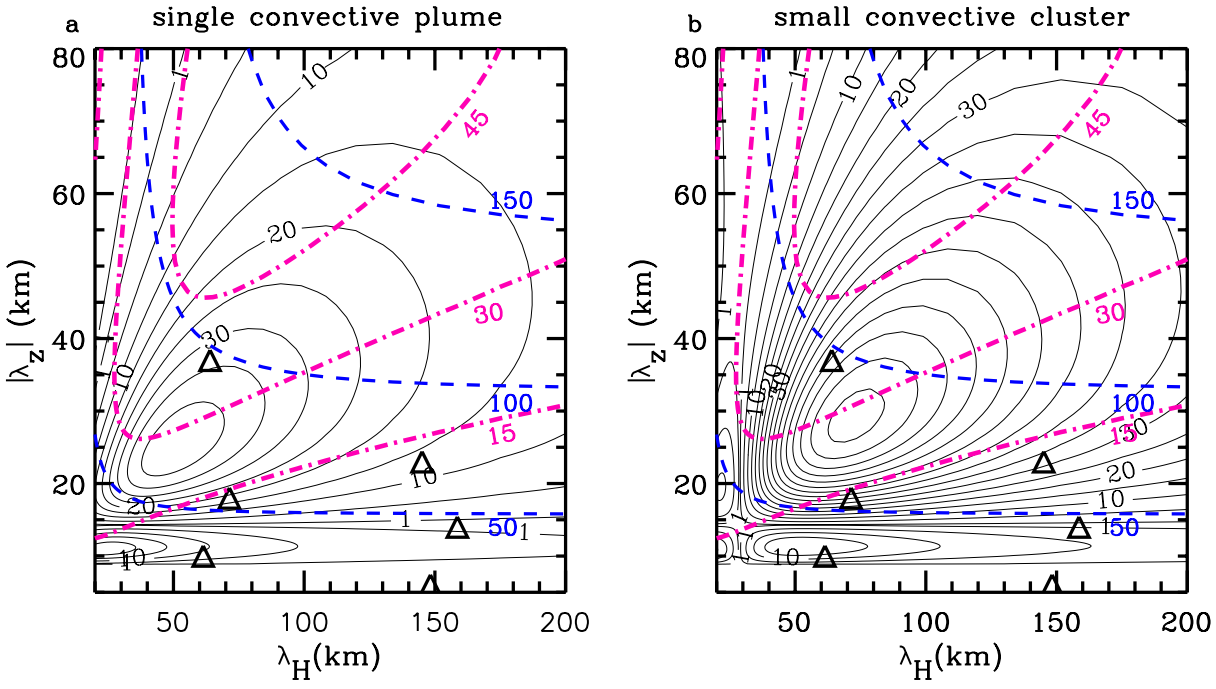

Fig. 18. GW horizontal velocity amplitudes at z=87 km in intervals of 5 m/s (solid black lines). An additional contour line at 1 m/s is also shown. These amplitudes are the maximum wave amplitudes. **(a)** Single convective plume envelope that is 20 km wide, 10 km deep, and lasts for 12 min. **(b)** Small convective cluster consisting of 3 of the same plumes from a), but arranged in a triangle configuration. Dash-dot pink lines indicate the vertical group velocity, c_{gz}, in 15 ms^{-1} intervals, as labeled. Dash blue lines indicate the intrinsic horizontal phase speed, c_{IH}, for 50, 100, and 150 ms^{-1}, as labeled. The triangles show the observed medium-scale GWs, where λ_z are calculated at the tropopause from ray tracing through the model winds.

consists of 3 convective plumes, each of which is identical to the convective plume in Fig. 18a, but which form the corners of a triangle with sides of 20 km (Vadas and Fritts, 2009). These plumes are in phase, moving upwards at the same time. We see that the model amplitudes for this small convective cluster are ∼2 times larger than for the single convective plume. The model amplitudes coresponding to the observed GWs (at the location of the triangles) are shown in the second column of Table 6.

Figure 18 shows that medium-scale GWs with c_{IH}>100 m/s and λ_z>50 km are excited from a single convective plume envelope with a maximum amplitude of order $u'_H \leq$20 m/s. Why then were these faster, medium-scale GWs not observed during this experiment? Because these fast GWs are steeply propagating, their convective sources would have been very close, ∼80–200 km away from the all-sky imager. However, old cloud material (i.e. anvils), tend to build up and move downstream with the upper-level tropospheric winds, away from active convective areas. For example, in Fig. 9, we see old cloud material spread out around the active convective updrafts by 100–200 km. Therefore, we hypothesize that when deep convective sources were less than 200 km from the all-sky imager, the large anvils that are formed from previous convective plumes in the same area prevented these faster and steeper GWs from being observed by the all-sky imager due to cloudy conditions.

7 Conclusions

In this paper, we investigated the sources of the 6 medium-scale GWs observed by Taylor et al. (2009) in the OH airglow layer during the SpreadFEx. We focused on medium scale GWs, rather than small scale GWs, because small-scale GWs tend to have smaller phase speeds, which are particularly sensitive to uncertainties in the horizontal winds in the OH layer and below; therefore, reverse ray tracing small-scale GWs from the OH layer to the tropospause is more difficult for source identification and quantification than reverse ray tracing medium-scale GWs with large horizontal phase speeds. We note that the Taylor et al. (2009) study is one of the first studies to observe medium-scale GWs in the OH layer. Other recent studies to do so are Takahashi et al. (2008) and Shiokawa et al. (2008).

Satellite images were available nearly every 30 min on 30 September and 1 October. Not surprisingly, good ray trace "fits" were obtained on these days when the uncertainties in the source locations and times were small. For the other days, satellite images were only available every 3 h. Using infrared

satellite images, we found that in late September and early October, convection was located primarily to the west, northwest, and southwest of Brasilia. In late October, convection was primarily located to the northwest and west of Brasilia. These directions correspond well with the propagation directions of the small and medium-scale GWs observed by Taylor et al. (2009) in the OH airglow layer.

We then reverse ray traced each GW from the OH layer back to the tropopause using zero winds and the model winds. The temperature and wind model was based on meteor radar wind data, temperature and winds from balloon soundings at lower altitudes, and temperature and winds from the TIME-GCM. The time and range from the OH layer to the source depended on the GW characteristics and winds. We found that 4 of the 6 medium-scale GWs ray traced to or very near active convective regions, as detailed below, and were therefore likely excited from deep convection. Although we attempted to pinpoint the exact convective plumes and clusters which generated these GWs, we could only do so for two of the GWs. For the other two GWs, we were still able to identify the localized convective regions which likely excited these GWs. The other 2 of the 6 GWs were also probably excited from deep convection; however, if so, they must have been ducted 500–700 km (Walterscheid et al., 1999; Hecht et al., 2001). We note that the medium-scale GWs at Cariri did not reverse ray trace to convective sources, but rather to regions where there was strong vertical motion of the air (Wrasse et al., 2009); therefore, the GWs observed in the OH layer above Brasilia and Cariri appear to have different sources during this experiment.

We now summarize the results of our reverse ray trace studies:

- The medium scale GW observed on the night of 30 September–1 October (with λ_H=145.1 km) reverse ray traced to within 100 km of a deep convective plume at 52^o W and 16.5^o S at ∼01:00 UT on 1 October. According to the ray trace results, the "best-fit" occurs if the GW was excited propagating upwards initially through the model winds to the OH layer.

- The medium scale GW observed on the night of 1–2 October with λ_H=71.4 km reverse ray traced to within 0–10 km of a deep convective plume at 52.5^o W and 15^o S at ∼21:20 UT. According to the ray trace results, the "best-fit" occurs if the GW was excited propagating downwards initially, reflected off the Earth's surface, then propagated upwards through zero winds to the OH layer. This is our best fit for all of the medium-scale GWs.

- The medium scale GW observed on the night of 1–2 October with λ_H=158.6 km reverse ray traced to within 20–100 km of a convective plume or a small convective cluster located at $57-60^o$ W and $12-15^o$ S from 19:00–21:00 UT. Because of location and time uncertainties, this GW may have been initially downward or upward-propagating. Both the model winds and zero winds comprise good fits.

- The medium scale GW observed on the night of 22–23 October with λ_H=64.0 km reverse ray traced to a location 500–700 km short of a few deep convective plumes (along the same propagation direction) at longitudes of $-52-54^o$ and latitudes of $-6-7^o$ at ∼24:00 UT. We conclude that this GW was probably ducted 500–700 km horizontally before reaching the OH layer over the all-sky imager, if its source was convection.

- The medium scale GW observed on the night of 23–24 October with λ_H=61.4 km reverse ray traced to within 50–100 km of the nearest deep convective plumes at longitudes of $-50-53^o$ and latitudes of $-8-10^o$ at 16:00–21:00 UT. Note that at this time, there were many deep convective plumes within this area. Because of time and location uncertainties, this GW could have been initially upward or downward-propagating, and both the zero wind and model winds comprise good fits.

- The medium scale GW observed on the night of 23–24 October with λ_H=148.3 km reverse ray traced to a source location 700 km short of a small convective cluster at -1^o latitude and -62.5^o longitude at ∼09:00 UT. The "best-fit" model implies that the GW was probably initially downward-propagating, reflected off the Earth's surface, propagated upwards through zero winds, then was ducted 700 km before reaching the OH layer above the all-sky imager.

We also forward ray traced the medium-scale GWs from the OH layer into the thermosphere. We found that 2 of the waves, the GWs with λ_H=61.4 and 148.3 km, did not penetrate very far above the turbopause at z∼110 km. This was not surprising, because these GWs had slow horizontal phase speeds of c_H<30 m s^{-1}. Although very sensitive to the chosen wind model, we found that the GWs with λ_H=145.1 and 64 km likely did not penetrate above $z\simeq$165 km. However, we found that two of the GWs, those with λ_H=71.4 and 158.6 km, may have penetrated to $z\gtrsim$170 km, which is high enough to potentially seed equatorial spread F (ESF) or plasma bubbles $\sim\pm10^o$ from the magnetic equator, where the field lines are lower than at the magnetic equator. Since these waves would have reached z∼170 km only $3-6^o$ south of the magnetic equator, they may not have reached a high enough altitude at that magnetic latitude to seed ESF, however. We note that several of the medium-scale GWs identified by Takahashi et al. (2008) forward ray traced to near the bottomside of the F layer, using a wind model similar to that in this paper, except using the meteor radar winds at CA only. Takahashi et al. (2008) found that the horizontal scale of the measured GWs in the OH layer compared well with the

inter plasma-bubble distances in the ionosphere, suggesting a direct link between these GWs and the seeding of plasma bubbles.

Although many of the observed medium-scale GWs do not forward ray trace to the bottomside of the F layer, they are still indicators that other convectively-generated GWs with similar λ_H but with larger λ_z (which are more able to penetrate into the F-region (Vadas, 2007; Fritts and Vadas, 2008)) were likely excited as well (see Fig. 18). However, these larger-λ_z GWs would reach z=90 km closer (horizontally) to the source, because they have much larger intrinsic frequencies (Gossard and Hooke, 1975). These GWs would therefore reach z=90 km at a distance 100–200 km from the deep convective plume which excited them, whereas GWs with smaller λ_z might propagate 100s to 1000 km before reaching z=90 km. Because of the anvil clouds, which spread out horizontally from previous convective updrafts, these large-λ_z GWs might not be visible in the OH layer because of cloudy conditions. Therefore, it may be difficult to observe these medium-scale GWs with large λ_z that are energetic enough to reach the bottomside of the F layer, unless tropospheric winds are situated so as to blow the anvil clouds away from the imager location.

Finally, we found that the amplitudes of three of these medium-scale GWs agree well with our convective plume model. However, the GWs with $\lambda_H > 100$ km and $\lambda_z < 15$ km do not agree well with the plume or cluster model amplitudes; the model amplitudes are much smaller than the observed amplitudes. This is in a region of the GW spectrum where there is partial cancellation of wave amplitudes from ground reflection. Therefore, it is possible that the GWs with large λ_H and small $\lambda_z \lesssim 15$ km are not well represented by this convective plume model. Indeed, it has only been successfully tested on GWs observed in the OH airglow layer with $\lambda_H \sim 20-100$ km and $\lambda_z \sim 20-40$ km (Vadas et al., 2009).

Acknowledgements. This research was supported by NASA under contracts NNH07CC81C, NNH04CC67C, and NAS5-02036, and by AFOSR contract FA9550-06-C-0129. The authors would like to thank Ray Roble for the TIME-GCM data, and the anonymous reviewers for helpful comments.

Topical Editor U.-P. Hoppe thanks two anonymous referees for their help in evaluating this paper.

References

Baker, D. J. and Stair Jr., A. T.: Rocket measurements of the altitude distributions of the hydroxyl airglow, Phys. Scripta, 37, 611–622, 1998.

Batista, P. P., Clemesha, B. R., Tokumoto, A. S., and Lima, L. M.: Structure of the mean winds and tides in the meteor region over Cachoeira Paulista, Brazil (22.7^o S, 45^o W) and its comparison with models, J. Atmos. Solar Terr. Phys., 66(6–9), 623–636, 2004.

Bluestein, H. B., McCaul Jr., E. W., Byrd, G. P., and Woodall, G. R.: Mobile sounding observations of a tornadic storm near the dryline: The Canadian, texas storm of 7 May 1986, Mon. Weather Rev., 116, 1790–1804, 1988.

Bluestein, H. B.: Synoptic-Dynamic Meteorology in Midlatitudes. Volume II: Observations and Theory of Weather Systems, p. 444, 594 pp., 1993.

Boville, B. A.: Middle atmosphere version of CCM2 (MACCM2): Annual cycle and interannual variability, J. Geophys. Res., 100, 9017–9039, 1995.

Buriti, R. A., Hocking, W. K., Batista, P. P., Medeiros, A. F., and Clemesha, B. R.: Observations of equatorial mesospheric winds over Cariri (7.4 S) by a meteor radar and comparison with existing models, Ann. Geophys., 26, 485–497, 2008, http://www.ann-geophys.net/26/485/2008/.

Cowling, D. H., Webb, H. D., and Yeh, K. C.: Group rays of internal gravity waves in a wind-stratified atmosphere, J. Geophys. Res., 76, 213–220, 1971.

Dalgarno, A. and Smith, F. J.: The thermal conductivity and viscosity of atomic oxygen, Planet. Space Sci., 9, 1–2, 1962.

Dewan, E. M., Picard, R. H., ONeil, R. R., Gardiner, H. A., Gibson, J., Mill, J. D., Richards, E., Kendra, M., and Gallery, W. O.: MSX satellite observations of thunderstorm-generated gravity waves in mid-wave infrared images of the upper stratosphere, Geophys. Res. Lett., 25, 939–942, 1998.

Ejiri, M. K., Shiokawa, K., Ogawa, T., Igrashi, K., Nakamura, T., and Tsuda, T.: Statistical study of short-period gravity waves in OH and OI nightglow images at two separated sites, J. Geophys. Res., 108(D21), 4679, doi:10.1029/2002JD002795, 2003.

Forbes, J. M.: Tidal and planetary waves, in: The Upper Mesosphere and Lower Thermosphere: A Review of Experiment and Theory, edited by: Johnson, R. M. and Killeen, T. L., p. 356, American Geophysical Union, 1995.

Francis, S. H.: A theory of medium-scale traveling ionospheric disturbances, J. Geophys. Res., 79, 5245–5260, 1974.

Fritts, D. C. and Alexander, M. J.: Gravity wave dynamics and effects in the middle atmosphere, Rev. Geophys., 41(1), 1003, doi:10.1029/2001RG000106, 2003.

Fritts, D. C. and Vadas, S. L.: Gravity wave penetration into the thermosphere: sensitivity to solar cycle variations and mean winds, Ann. Geophys., 26, 3841–3861, 2008, http://www.ann-geophys.net/26/3841/2008/.

Fritts, D. C., Vadas, S. L., Riggin, D. M., Abdu, M. A., Batista, I. S., Takahashi, H., Medeiros, A., Kamalabadi, F., Liu, H.-L., Fejer, B. J., and Taylor, M. J.: Gravity wave and tidal influences on equatorial spread F based on observations during the Spread F Experiment (SpreadFEx), Ann. Geophys., 26, 3235–3252, 2008, http://www.ann-geophys.net/26/3235/2008/.

Fritts, D. C., Abdu, M. A., Batista, B. R., Batista, I. S., Batista, P. P., Buriti, R., Clemesha, B. R., Dautermann, T., de Paula, E., Fechine, B. J., Fejer, B., Gobbi, D., Haase, J., Kamalabadi, F., Kherani, E. R., Laughman, B., Lima, P. P., Liu, H.-L., Medeiros, A., Pautet, D., Riggin, D. M., Rodrigues, F. S., São Sabbas, F. T., Sobral, J. H. A., Stamus, P., Takahashi, H., Taylor, M. J., Vadas, S. L., Vargas, F., and Wrasse, C.: Overview and Summary of the Spread F Experiment (SpreadFEx), Ann. Geophys., in review, 2009.

Gerrard A. J., Kane, T. J., Eckermann, S. D., and Thayer, J. P.: Gravity waves and mesospheric clouds in the summer middle atmo-

sphere: A comparison of lidar measurements and ray modeling of gravity waves over Sondrestrom, Greenland, J. Geophys. Res., 109, D10103, doi:10.1029/2002JD002783, 2004.

Gossard, E. E. and Hooke, W. H.: Waves in the atmosphere, Elsevier Scientific Publishing Co., Amsterdam, 456 pp, 1975.

Hecht, J. H., Walterscheid, R. L., Hickey, M., and Franke, S.: Climatology and modeling of quasi-monochromatic atmospheric gravity waves observed over Urbana Illinois, J. Geophys. Res., 106(D6), 5181–5195, 2001.

Hecht, J. H., Kovalam, S., May, P. T., Mills, G., Vincent, R. A., Walterscheid, R. L., and Woithe, J.: Airglow imager observations of atmospheric gravity waves at Alice Springs and Adelaide, Australia during the Darwin Area Wave Experiment (DAWEX), J. Geophys. Res., 109, D20S05, doi:10.1029/2004JD004697, 2004.

Heymsfield, G. M. andBlackmer Jr., R. H.: Satellite-observed characteristics of midwest severe thunderstorm anvils, Mon. Weather Rev., 116, 2200–2224, 1988.

Hines, C. O.: On the nature of travelling ionospheric disturbances launched by low-altitude nuclear explosions, J. Geophys. Res., 72, 1877–1882, 1967.

Hocking, W, K., Fuller, B., and Vandepeer, B.: Real-time determination of meteor-related parameters utilizing modern digital technology, J. Atmos. Terr. Phys., 63(2–3), 155–169, 2001.

Hung, R. J. and Kuo, J. P.: Ionospheric observation of gravity-waves associated with hurricane Eloise, J. Geophys., 45, 67–80, 1978.

Hung, R. J. and Smith, R. E.: Ray tracing of gravity waves as a possible warning system for tornadic storms and hurricanes, J. Appl. Meteor., 17, 3–11, 1978.

Isler, J. R, Taylor, M. J., and Fritts, D. C.: Observational evidence of wave ducting and evanescence in the mesosphere, J. Geophys. Res., 102, 26 301–26 313, 1997.

Jones, W.: Ray Tracing for Internal Gravity Waves, J. Geophys. Res., 74(8), 2028–2033, 1969.

Kundu, P.: Fluid Dynamics, Academic Press, San Diego, 638 pp, 1990.

Lighthill, J.: Waves in Fluids, Cambridge University Press, Cambridge, 504 pp., 1978.

Lin, Y. and Zhang, F.: Tracking Gravity Waves in Baroclinic Jet-Front Systems, J. Atmos. Sci., 65, 2402–2415, doi:10.1175/2007JAS2482.1, 2008.

Lindzen, R. S.: Turbulence and stress owing to gravity wave and tidal breakdown, J. Geophys. Res., 86, 9707–9714, 1981.

Liu, A. Z. and Swenson, G. R.: A modeling study of O_2 and OH airglow perturbations induced by atmospheric gravity waves, J. Geophys. Res., 108, 11-1–11-9, doi:10.1029/2002JD002474, 2003.

Marks, C. J. and Eckermann, S. D.: A three-dimensional nonhydrostatic ray-tracing model for gravity waves: Formulation and preliminary results for the middle atmosphere, J. Atmos. Sci., 52, 1959–1984, 1995.

Medeiros, A. F., Taylor, M. J., Takahashi, H., Batista, P. P., and Gobbi, D.: An investigation of gravity wave activity in the lower-latitude upper mesopause: Propagation direction and wind filtering, J. Geophys. Res., 108(D14), 4411, doi:10.1029/2002JD002593, 2003.

Menzel, W. P. and Purdom, J. F. W.: Introducing GOES-I: The first of a new generation of geostationary operational environmental satellites, B. Am. Meteorol. Soc., 75, 757–781, 1994.

Midgley, J. E. and Liemohn, H. B.: Gravity waves in a realistic atmosphere, J. Geophys. Res., 71, 3729–3748, 1966.

Nakamura, T., Higashikawa, A., Tsuda, T., and Matsushita, Y.: Seasonal variations of gravity wave structures in OH airglow with a CCD imager at Shigaraki, Earth Planets Space, 51, 897–906, 1999.

Nielsen, K., Taylor, M. J., Pautet, P. D., Fritts, D. C., Mitchell, N., Beldon, C., Singer, W., Schmidlin, F. J., and Goldberg, R. A.: Propagation of short-period gravity waves at high-latitudes during the MaCWAVE winter campaign, Ann. Geophys., 24, 1227–1243, 2006,
http://www.ann-geophys.net/24/1227/2006/.

Pautet, P.-D., Taylor, M. J., Liu, A. Z., and Swenson, G. R.: Climatology of shot-period gravity waves observed over northern Australia during the Darwin Area Wave Experiment (DAWEX) and their dominant source regions, J. Geophys. Res., 110, D03S90, doi:10.1029/2004JD004954, 2005.

Roble, R. G. and Ridley, E. C.: A thermosphere-ionosphere-mesosphere-electrodynamics general circulation model (TIME-GCM): equinox solar cycle minimum simulations (30–500 km), Geophys. Res. Lett., 21, 417–420, 1994.

Roble, R. G.: Energetics of the mesosphere and thermosphere, in: The Upper Mesosphere and Lower Thermosphere: A Review of Experiment and Theory, edited by: Johnson, R. M. and Killeen, T. L., Geophysical Monograph Series., American Geophysical Union, 87, 356 p., 1995.

Samson, J. C., Greenwald, R. A., Ruohoniemi, J. M., Frey, A., and Baker, K. B.: Goose Bay Radar observations of Earth-reflected atmospheric gravity waves in the high-latitude ionosphere, J. Geophys. Res., 95, 7693–7709, 1990.

São Sabbas, F. T., Rampinelli, V. T., Santiago, J., Stamus, P., Vadas, S., and Dolif Neto, G.: Characterization of convective gravity wave sources in satellite IR imagery, Ann. Geophys, in review, 2009.

Sentman, D. D., Wescott, E. M., Picard, R. H., Winick, J. R., Stenbaek-Nielsen, H. C., Dewan, E. M., Moudry, D. R., São Sabbas, F. T., Heavner, M. J., and Morrill, J.: Simultaneous observations of mesospheric gravity waves and sprites generated by a midwestern thunderstorm, J. Atmos. Solar Terr. Phys., 65, 537–550, 2003.

Shiokawa, K., Otsuka, Y., and Ogawa, T.: Propagation characteristics of nighttime mesospheric and thermospheric waves observed by optical mesosphere thermosphere imagers at middle and low latitudes, Earth Planets Space, in press, 2008.

Smith, S. M., Mendillo, M., Baumgardner, J., and Clark, R. R.: Mesospheric gravity wave imaging at subauroral site: First results from Millstone Hill, J. Geophys. Res., 106, 27 119–27 130, 2000.

Snively, J. B., Pasko, V. P., Taylor, M. J., and Hocking, W. K.: Doppler ducting of short-period gravity waves by mid-latitude tidal wind structure, J. Geophys. Res., 112, A03304, doi:10.1029/2006JA011895, 2007.

Suzuki, S., Shiokawa, K., Otsuka, Y., Ogawa, T., Nakamura, K., and Nakamura, T.: A concentric gravity wave structure in the mesospheric airglow images, J. Geophys. Res., 112, D02102, doi:10.1029/2005JD006558, 2007.

Swenson, G. R. and Mende, S. B.: OH emissions and gravity waves (including a breaking wave) in all-sky imagery from Bear Lake, Utah, Geophys. Res. Lett., 21, 2239–2242, 1994.

Takahashi, H., Taylor, M. J., Pautet, P.-D., Medeiros, A. F., Gobbi, D., Wrasse, C. M., Fechine, J., Abdu, M. A., Batista, I. S., Paula, E., Sobral, J. H. A., Arruda, D., Vadas, S. L., Sabbas, F. S., and Fritts, D. C., Simultaneous observation of ionospheric plasma bubbles and mesospheric gravity waves during the SpreadFEx Campaign, Ann. Geophys., submitted, 2008.

Taylor, M. J., Bishop, M. B., and Taylor, V.: All-sky measurements of short period waves imaged in the OI (557.7 nm), Na(589.2 nm) and near infared OH and O_2(0,1) nightglow emissions during the ALOHA-93 campaign, Geophys. Res. Lett., 22, 2833–2836, 1995.

Taylor, M. J., Pendleton Jr., W. R., Clark, S., Takahashi, H., Gobbi, D., and Goldberg, R. A.: Image measurements of short-period gravity waves at equatorial latitudes, J. Geophys. Res., 102, 26 283–26 299, 1997.

Taylor, M. J. and Hapgood, M. A.: Identification of a thunderstorm as a source of short period gravity waves in the upper atmospheric nightglow emissions, Planet. Space Sci., 36, 975–985, 1988.

Taylor, M. J., Pautet, P.-D., Medeiros, A. F., Buriti, R. A., Fechine, J., Fritts, D. C., Vadas, S. L., Takahashi, H., and São Sabbas, F. T.: Characteristics of mesospheric gravity waves near the magnetic equator, Brazil during the SpreadFEx campaign, Ann. Geophys., in press, 2009.

Vadas, S. L., Fritts, D. C., and Alexander, M. J.: Mechanism for the generation of secondary waves in wave breaking regions, J. Atmos. Sci., 60, 194–214, 2003.

Vadas, S. L. and Fritts, D. C.: Thermospheric responses to gravity waves arising from mesoscale convective complexes, J. Atmos. Solar Terr. Phys., 66, 781–804, 2004.

Vadas, S. L. and Fritts, D. C.: Thermospheric responses to gravity waves: Influences of increasing viscosity and thermal diffusivity, J. Geophys. Res., 110, D15103, doi:10.1029/2004JD005574, 2005.

Vadas, S. L. and Fritts, D. C.: Influence of solar variability on gravity wave structure and dissipation in the thermosphere from tropospheric convection, J. Geophys. Res., 111, A10S12, doi:10.1029/2005JA011510, 2006.

Vadas, S. L.: Horizontal and vertical propagation and dissipation of gravity waves in the thermosphere from lower atmospheric and thermospheric sources, J. Geophys. Res., 112, A06305, doi:10.1029/2006JA011845, 2007.

Vadas, S. L. and Fritts, D. C.: Reconstruction of the gravity wave field from convective plumes via ray tracing, Ann. Geophys., 27, 147–177, 2009, http://www.ann-geophys.net/27/147/2009/.

Vadas, S. L., Yue, J., She, C.-Y., Stamus, P. A., and Liu, A. Z.: A model study of the effects of winds on concentric rings of gravity waves from a convective plume near Fort Collins on 11 May 2004, J. Geophys. Res., in press, doi:10.1029/2008JD010753, 2009.

Volland, H.: Full wave calculations of gravity wave propagation through the thermosphere, J. Geophys. Res., 74, 1786–1795, 1969.

Waldock, J. A. and Jones, T. B.: The effects of neutral winds on the propagation of medium-scale atmospheric gravity waves at mid-latitudes, J. Atmos. Terr. Phys., 46, 217–231, 1984.

Waldock, J. A. and Jones, T. B.: Source regions of medium scale travelling ionospheric disturbances observed at mid-latitudes, J. Atmos. Terr. Phys., 49, 105–114, 1987.

Walterscheid, R. L., Hecht, J. H., Vincent, R. A., Reid, I. M., Woithe, J., and Hickey, M. P.: Analysis and interpretation of airglow and radar observations of quasi-monochromatic gravity waves in the upper mesosphere and lower thermosphere over Adelaide, Australia (35^o S, 138^o E), J. Atmos. Solar Terr. Phys., 61, 461–478, 1999.

Wrasse, C. M., Takahashi, H., Fechine, J., Medeiros, A. F., and Bageston, J. V.: Mesospheric Gravity Wave Observations during the SpreadFEX Campaign: Evidence of Tropospheric Sources, Ann. Geophys., in review, 2009.

Yanowitch, M.: Effect of viscosity on gravity waves and the upper boundary condition, J. Fluid Mech., 29, 209–231, 1967.

Yeh, K. C., Liu, C. H., and Youakim, M. Y.: Attenuation of internal gravity waves in model atmospheres, Ann. Geophys., 31, 321–328, 1975, http://www.ann-geophys.net/31/321/1975/.

Yue, J., Vadas, S. L., She, C.-Y., Nakamura, T., Reising, S., Liu, H.-Li, Stamus, P., Krueger, D., Lyons, W., and Li, T.: Concentric gravity waves in the mesosphere generated by deep convective plumes in the lower atmosphere near Fort Collins, CO, J. Geophys. Res., in press, doi:10.1029/2008JD011244, 2009.